FULL PAPER

Advanced Solute Conservation Equations for Dendritic Solidification Processes Part II: Numerical Simulations and Comparisons

Mostafa Omar El-Bealy

The mathematical model of derived solute equations in part I for equiaxed dendritic solidification with melt convection streams and interdendritic thermo-metallurgical strain is applied numerically to predict macrosegregation distributions with different diffusing mechanisms in dendritic solid. Numerical and experimental results are present for solidification of a Al–4.5% Cu alloy inside horizontal rectangular cavity at different superheats. The numerical simulations were performed by using simpler method developed by Patanker. The experiments were conducted to measure the cooling curves via thermocouples and the metallurgical examinations to measure the grain size and macrosegregation distributions in Part I. Preliminary validity of the model is demonstrated by the qualitative and quantitative agreements between the measurements and predications of cooling curves and predicted macrosegregation distributions including mushy permeability and interdendritic strain. In addition, several important features of macrosegregation in equiaxed dendritic solidification are identified through this combined experimental and numerical study. Also, quantitative agreements between the numerical simulations and experiments reveal several areas for future research work. The differences and errors between predicted macrosegregation results under different diffusing mechanisms have been discussed.

1. Introduction

In recent years, numerical simulations of macrosegregation phenomena have experienced considerable progress. Solidification phenomena and interdendritic liquid convection streams have been coupled with transient heat conduction calculations to determine the different types of macrosegregation phenomena.[1–7] However, simulations of macrosegregation during dendritic solidification, taking interdendritic strain and mushy permeability have not been much attempted in the literature, with exception being the experimental and theoretical studies by El-Bealy and Fredriksson.[8–10] These studies include the effect of both interdendritic strain but deals with a complete diffusion in dendritic solid only.

This second article of two parts paper describes a first attempt towards predicting macrosegregation in the presence of interdendritic strain and mushy permeability under different diffusion mechanisms in dendritic solid using the governing equations developed by El-Bealy and described in Part I of this paper. The macrosegregation features of particular interest include the effects of thermal convection streams which is an index measuring how the solute liquid move between the equiaxed crystals. In addition, it is interest to predict movement of interdendritic liquid as a result of combined effects of mushy permeability and interdendritic strain.

In the following sections, experimental and theoretical system is briefly outlined for completeness. This is then followed by a description of numerical procedures. Representative numerical results of 2D mathematical model are finally presented to shed light on the complicated different phenomena occurring during solidification of dendritic alloy particularly in equiaxed dendritic structure.

Prof. Mostafa Omar El-Bealy is a Chair Professor of Materials Processing & Technology for Companies, Chair in MTC/Egypt, CTU/Germany, KTH/Sweden and MIT/USA. Prof. El-Bealy is now with Egypt branch of this chair temporally.
Email: moelbealy@hotmail.com

2. Experimental and Theoretical System Description

The experimental and theoretical system considered deals with solidification of an Al–4.5% Cu alloy in a two-dimensional (2D) horizontal rectangular cavity of length 0.08 m and of height 0.04 m, as shown in **Figure 1**. The melt has an initial temperature of 938, 968, and 993 K, for different superheats 20, 50, and 75 K, respectively, and initial concentration of 4.5 wt pct copper. The walls are impermeable and adiabatic except the right wall which is subjected to cooling system for $t > 0$. The cooling temperature is fixed at 298 K in all simulations presented. This set of parameters is representative of practical casting conditions and falls into the range of equiaxed dendritic solidification, as given by Fredriksson and. Olsson.[11]

The mathematical approach which has been developed from the first principles to model the general frame-work for governing equations continuity, momentum,[12] heat transfer presented by Poirier and coworkers,[13] interdendritic thermo-metallurgical strain and macrosegregation developed by El-Bealy.[10,14,15] Most of these equations are chosen for simplicity and could be changed without introducing fundamentals changes to the model. Only a few explanations are provided here, and the reader is referred to the original references for the details of the model derivations, assumptions, and properties of

aluminum alloy. The model equations together with supplementary relations presented therein are again summarized in 2D form in Table **1–3**. All symbols are defined in the nomenclature in the end of this article. The model presentation is divided into three parts.

In the second part of this study, transport equations including continuity, momentum, and heat transfer have been reformulated in two-dimensional forms as shown in **Table 1**. It is assumed that viscosity and density are constant as well as the body force is negligible in the x-direction whereas in the case of z-direction, body force is replaced by gravitational force ρg as shown in Equations T-1-2 and T-1-3, respectively.[12] Therefore, it is convenient to write momentum equations in the form of Navier stoke equations shown in Equations T-1-1 to T-1-3.[12] However, Poirier et al.[13] approach was used to model a heat transfer of dendritic solidification and it has been thoroughly discussed in Ref. [13] The model distinguishes the heat transfer in liquid, mushy, and solid zones taken into account the effects of heat of mixing in both the dendritic solid and the interdendritic liquid in the mushy zone and also the effects of heat changes of different solid phase transformations in the solid zone. Therefore, the intensive enthalpy $\bar{H}$ is written with an overbar to emphasize that there is microsegregation of solute in the local dendritic solid, so that its intensive enthalpy is an average in Equations T-1-4 to T-1-6. One of the important assumptions made in this
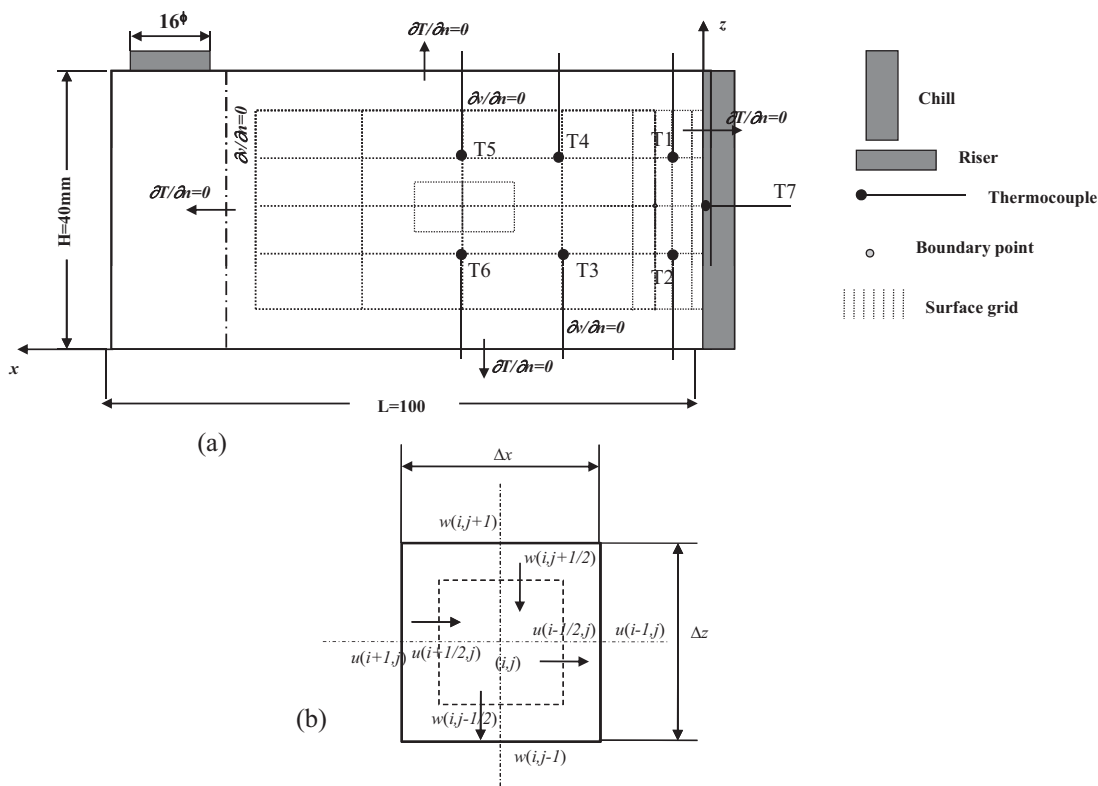

Figure 1. Schematic illustration of a) grid of computations and b) control volume of 2D situation.

Transport equations

Continuity equation[12]

$$\frac{\partial \rho}{\partial t} + \frac{\partial}{\partial x}(\rho u) + \frac{\partial}{\partial z}(\rho w) = 0 \qquad \text{T-1-1}$$

Momentum equations (Navier stokes equations)[12]

$$\rho \frac{\partial u}{\partial t} + \rho u \frac{\partial u}{\partial x} + \rho w \frac{\partial u}{\partial z} - \mu\left(\frac{\partial^2 u}{\partial x^2} + \frac{\partial^2 u}{\partial z^2}\right) = -\frac{\partial P}{\partial x} \qquad \text{T-1-2}$$

$$\rho \frac{\partial w}{\partial t} + \rho u \frac{\partial w}{\partial x} + \rho w \frac{\partial w}{\partial z} - \mu\left(\frac{\partial^2 w}{\partial x^2} + \frac{\partial^2 w}{\partial z^2}\right) = \rho g - \frac{\partial P}{\partial z} \qquad \text{T-1-3}$$

Energy equation "Poirier model"[13]

For Mushy region

$$\bar{\rho}\frac{\partial \bar{H}_s}{\partial t} + A_l \rho_l \frac{\partial L}{\partial t} - L\frac{\partial}{\partial t}(A_s \rho_s) = \lambda_{\text{eff}}\left(\frac{\partial^2 T}{\partial x^2} + \frac{\partial^2 T}{\partial z^2}\right) - \rho_l U\left[\left(\frac{\partial \bar{H}_s}{\partial x} + \frac{\partial \bar{H}_s}{\partial z}\right) + \left(\frac{\partial L}{\partial x} + \frac{\partial L}{\partial z}\right)\right] \qquad \text{T-1-4}$$

For liquid region

$$\frac{\partial H_l}{\partial t} = \frac{\lambda_l}{\rho_l}\left(\frac{\partial^2 T}{\partial x^2} + \frac{\partial^2 T}{\partial z^2}\right) - U\left(\frac{\partial H_l}{\partial x} + \frac{\partial H_l}{\partial z}\right) \qquad \text{T-1-5}$$

For solid region

$$\frac{\partial}{\partial t}(\rho_s \bar{H}_s) = \lambda_s\left(\frac{\partial^2 T}{\partial x^2} + \frac{\partial^2 T}{\partial y^2}\right) \qquad \text{T-1-6}$$

Solidification

Dendritic solid phase

For complete diffusion "Rogberg appraoch"[19]

$$A_s = \frac{1}{1-K^e}\left\{1 - \frac{K^e}{\frac{(T_l-T)(1-K^e)}{(T_l-T_s)} + K^e}\right\} \qquad \text{T-1-7}$$

For no and some diffusion "Scheil approach"[20]

$$A_s = 1 - \left(\frac{T-T_m}{T_l-T_m}\right)^{(1/K^e-1)} \qquad \text{T-1-8}$$

Table 1. Conversation equations of transport and solidification phenomena.

model is that the solid thermal conductivity is constant whereas in the case of liquid thermal conductivity in both in the liquid and mushy zones is considered including the effect of convection streams and melt superheat.[16,17] Also, the density functions of dendritic solid in mushy zone is considered as functions in local temperature and concentration of solute.[18]

Consequently, the solidification model discriminates different dendritic solid and interdendritic liquid phases in the mushy zone by using Rogberg[19] approach in the case of complete diffusion in dendritic solid whereas in the cases of no diffusion and some diffusion in dendritic solid, it can be used Scheil's[20] approach as shown in Equation T-1-7 and T-1-8, respectively.

The conservation equation of interdendritic thermo-metallurgical strain illustrated in Equation T-2-1[14] is governed by storage energy and volume change effects on the control volume element solidified within different regions

in the mushy zone.[8,10] These regions are incoherent and coherent mushy regions and governed by three thermal isotherms called coherent, liquidus, and solidus isotherms[21–23] as illustrated in Equations T-3-1 through T-3-4, respectively. The incoherent mushy region is bounded by liquidus and coherent isotherms whereas the coherent mushy region is bounded by coherent and solidus isotherms. Subsequently, the storage energy effect of Equation T-2-1 consists of three main parameters. These main parameters illustrate in the numerator of Equation T-2-1 whereas one parameter appears in the dominator. The numerator's parameters are transported energy Etr, see Equation T-3-5 and the second parameter is inner energy generated during solidification and cooling Ein as shown in Equation T-3-6.[14] Equation T-3-6 shows that the inner energy Ein which generates from three sources. The first source is energy generated due to change in the dendritic solid enthalpy Es and the second one is energy generated

Interdendritic Strain "El-Bealy model"[14]   T-2-1

$$\frac{d\varepsilon^{T_{ph}}}{dt} = \frac{\alpha\left[\lambda_{eff}\left(\frac{\partial^2 T}{\partial x^2} + \frac{\partial^2 T}{\partial z^2}\right)\right] + \frac{\partial}{\partial t}\sum_{\eta} E_{\eta}}{\bar{E}} + \frac{\left(\frac{V(T)}{V(T_{coh})}\right)^{1/3} - 1}{dt}$$

Macrosegregation "El-Bealy model"[8,10]

For complete diffusion

$$[A_l\rho_l + A_s\rho_s K^e(1 + \textstyle\sum\varepsilon_i)]\frac{\partial C_l}{\partial t} = C_l(1 - K^e)\left\{\left[\rho_s\frac{\partial A_s}{\partial t} + A_s\frac{\partial\rho_s}{\partial t}\right](1 + \textstyle\sum\varepsilon_i) + \rho_s A_s\frac{\partial\sum\varepsilon_i}{\partial t}\right\} - \rho_l A_l U\kappa\left(\frac{\partial C_l}{\partial x} + \frac{\partial C_l}{\partial z}\right)$$ T-2-2

For no diffusion

$$A_l\rho_l\frac{\partial C_l}{\partial t} = [(1 - K^e)(1 + \textstyle\sum\varepsilon_i)C_l\rho_l]\frac{\partial A_s}{\partial t} + [(1 + C_l K^e)(1 + \textstyle\sum\varepsilon_i)A_s]\frac{\partial\rho_s}{\partial t} + A_s\rho_s(1 - C_l K^e)\frac{\partial\sum\varepsilon_i}{\partial t} - \rho_l A_l U\kappa\left(\frac{\partial C_l}{\partial x} + \frac{\partial C_l}{\partial z}\right)$$ T-2-3

For some diffusion

$$\left(\rho_l A_l + 2\alpha^* \rho_s A_s K^e + 2\alpha^* \rho_s A_s K^e \textstyle\sum\varepsilon_i\right)\frac{\partial C_l}{\partial t} = \left(A_l\frac{\partial\rho_l}{\partial t} + \rho_l\frac{\partial A_l}{\partial t}\right)(1 - C_l) - \left(A_s\bar{C}_s\frac{\partial\rho_s}{\partial t} + \rho_s K^e C_l\frac{\partial A_s}{\partial t}\right)\left(1 + \textstyle\sum\varepsilon_i\right) -$$
$$A_s\rho_s K^e C_l\frac{\partial\sum\varepsilon_i}{\partial t} - \rho_l A_l U\kappa\left(\frac{\partial C_l}{\partial x} + \frac{\partial C_l}{\partial z}\right)$$ T-2-4

Segregation ratio

$$S_{Cu} = \frac{Cu_{meaured}}{Cu_{nominal}}$$ T-2-5

Table 2. Conversation equations of interdendritic strain and macrosegregation phenomena.

resulted from dendritic solid formation rate from liquid phase "$\frac{\partial f_s^i}{\partial t}$" whereas the third source is energy generated due to solid-state phase transformation from phase i–j "$\frac{\partial f_s^{i-j}}{\partial t}$". However, the average energy capacity $\bar{E}$ of control volume element with different phases appears in the dominator of Equation T-2-1 and is shown in Equation T-3-7. The second part of Equation T-1-7 represents the volume change strain rate associated with the shrinkage or thermal dendritic solid contraction shown in Equation T-3-8.[14,24] Therefore, the Part II of interdendritic strain equation was applied only in the incoherent mushy region to simulate thermo-metallurgical strain whereas the two parts of this equation were applied in the coherent mushy region.

Finally, three macroscopic model equations of solute redistribution under different diffusion mechanisms in dendritic solid derivative in Part I of this two parts paper can be simplified for two dimensional form and summarized them in **Table 2**. Effects of convection streams, mushy permeability, and interdendritic strain associated with dendritic solidification processes were taken into account. The first model equation describes the solute redistribution mechanism under complete diffusion in the dendritic solid and the second model demonstrates solute redistribution mechanism under no diffusion whereas the third one exhibits this mechanism under some diffusion in dendritic solid as shown in Equations T-2-2, T-2-3, and T-2-4 in Table 2, respectively. These equations show several important features. These features can be observed with regarded parameters in Equations T-2-2 to T-2-4 in Table 2: (i) the independent variable A_s in different macrosegregation equations will take values between 0 to A during the solidification where A is equal to unity in these computations. A_s can be formulated by a continu-

ous function of temperature used only with a complete diffusion in dendritic solid and this equation illustrated in Equation T-1-7.[19] However, in the case of no or same diffusion in dendritic solid, this variable in can be computed by using Scheil's equation shown in Equation T-1-8;[20] (ii) the total local velocity of interdendritic fluid flow relative to the solid "U_{Int}" including the thermal convection components "U_{Conv}", in the direction η "U_{η}" can be calculated from relations T-3-9 to T-3-11; (iii) describing convection through the mushy zone requires knowledge of the relationship between mushy permeability "κ" and mushy morphology such as grain size[25] and fraction of interdendritic liquid "A_l", etc. The Kozeny–Carman[26] relation for the permeability of packed beds of spheres "porous bed" illustrated in T-3-12 was used to measure mushy permeability of Al–4.5% Cu alloy.[26] The number density of grains is needed for the expression for grain boundary surface area per unit area "S_A" presented in Ref. [27]. In these calculations, the grain density is taken to be uniform and equal to average values for each control volume as determined from the experimental measurements in Part I.

3. Numerical Performance

3.1. Initial and Boundary Conditions

A schematic model domain is shown in Figure 1a and represents a longitudinal two-dimensional section 40 mm × 80 mm of cast ingot simulated in the present

Mushy coherent region[8,10]

Coherent temperature[1,3]

$$T_{\mathrm{coh}} = T_{\mathrm{s}} + f_{\mathrm{coh}}(T_{\mathrm{l}} - T_{\mathrm{s}})$$ T-3-1

Coherent fraction

$$f_{\mathrm{coh}} = \left\{ a - b\left(\frac{V_{\mathrm{a}}}{R_{\mathrm{d}}}\right) \right\}$$ T-3-2

Liquidus and solidus temperatures[21]

$$T_{\mathrm{l}} = T_{\mathrm{lo}} + \sum_{j=1}^{N_{\mathrm{e}}} \psi_j \chi_j^{\mathrm{l}}$$ T-3-3

$$T_{\mathrm{s}} = T_{\mathrm{so}} + \sum_{j=1}^{N_{\mathrm{e}}} \beta_j \chi_j^{\mathrm{l}}$$ T-3-4

Thermo-metallurgical strain characteristics[14]

$$\frac{\mathrm{d}E_{\mathrm{tr}}}{\mathrm{d}t} = -\alpha\left[\left(\frac{\partial}{\partial x}\left(-\lambda\frac{\partial T}{\partial x}\right)\right) + \left(\frac{\partial}{\partial z}\left(-\lambda\frac{\partial T}{\partial z}\right)\right)\right]$$ T-3-5

$$\frac{\mathrm{d}E_{\mathrm{in}}}{\mathrm{d}t} = \frac{\partial}{\partial t}\sum_i (f_i\rho_i H_i) = \frac{\partial}{\partial t}\left(f_{\mathrm{s}}\rho_{\mathrm{s}}\,\bar{H}_{\mathrm{s}} + f_{\mathrm{l}}^{\mathrm{l}\to\mathrm{s}}\rho_{\mathrm{l}}H_{\mathrm{l}} + f_{\mathrm{s}}^{i\to j}\rho_{\mathrm{s}}H_{i\to j}\right)$$ T-3-6

$$\bar{E} = f_{\mathrm{s}}\rho_{\mathrm{s}}\,\bar{H}_{\mathrm{s}} + f_{\mathrm{l}}\rho_{\mathrm{l}}H_{\mathrm{l}}$$ T-3-7

$$\frac{\left(\frac{\rho(T_{\mathrm{coh}})}{\rho(T)}\right)^{1/3} - 1}{\mathrm{d}t}$$ T-3-8

Interdendritic velocity[8]

Total velocity

$$U_\eta = U_{\mathrm{Int}}\eta \pm U_{\mathrm{Conv}}\eta$$ T-3-9

Interdendritic fluid velocity[8–10]

$$U_x = \frac{1}{A_{\mathrm{l}}\rho_{\mathrm{l}}}\int_{x_{\mathrm{s}}}^{x}\frac{\partial}{\partial t}(A_{\mathrm{l}}\rho_{\mathrm{l}} + A_{\mathrm{s}}\rho_{\mathrm{s}}(1 + \varepsilon_x))\mathrm{d}x$$ T-3-10

$$U_z = \frac{1}{A_{\mathrm{l}}\rho_{\mathrm{l}}}\int_{z_{\mathrm{s}}}^{z}\frac{\partial}{\partial t}(A_{\mathrm{l}}\rho_{\mathrm{l}} + A_{\mathrm{s}}\rho_{\mathrm{s}}(1 + \varepsilon_z))\mathrm{d}z$$ T-3-11

Mushy permeability[23]

$$\kappa = \frac{A_{\mathrm{l}}^3}{S_{\mathrm{A}}^2 k_{\mathrm{c}}(1 - A_{\mathrm{l}}^2)}$$ T-3-12

Table 3. Summary of supplement relations.

study. Figure 1 shows also the implicit finite-difference mash and its boundary conditions employed to simulate different thermal fields of a rectangular ingot section. A non-uniform grid system with $80\,\mathrm{mm} \times 40\,\mathrm{mm}$ was adopted and the domain comes into 28 nodes. The dimensions of control elements are $\Delta x = 5\,\mathrm{mm}$ for first 20 mm from the ingot surface, then changes into $\Delta x = 20\,\mathrm{mm}$ for rest of ingot length and $\Delta z = 10\,\mathrm{mm}$ for all grid mash of computations as shown in Figure 1a. Consequently, the initial conditions when $t = 0$, the temperature $T_\phi = T_{\mathrm{pour}}$.

Heat transfer at ingot surface was assumed to follow a generalized Newtonian law. Thus, it was assumed that heat flux across the ingot surface is proportional to the difference between ingot surface and water cooling constant temperatures as defined in Equation T-4-1. Therefore, for surface boundary conditions of $x = 0$, the surface ingot heat flux can be computed as represented in Equation T-4-2 illustrated in **Table 4**. For boundary conditions at $x = 80$, $z = 0$, $z = 40\,\mathrm{mm}$, the heat fluxes can be calculated from Equation T-4-3.

$Q_\phi = h(t)(T_\phi - T_{\mathrm{w}})$	T-4-1
$\lambda\left(\frac{\partial T}{\partial x}\right)_{x=0} = h(t)(T_\phi - T_{\mathrm{w}})$	T-4-2
$\lambda\left(\frac{\partial T}{\partial x}\right)_{x=80} = 0,\ \lambda\left(\frac{\partial T}{\partial z}\right)_{z=0} = 0$ and $\lambda\left(\frac{\partial T}{\partial z}\right)_{z=40} = 0$	T-4-3

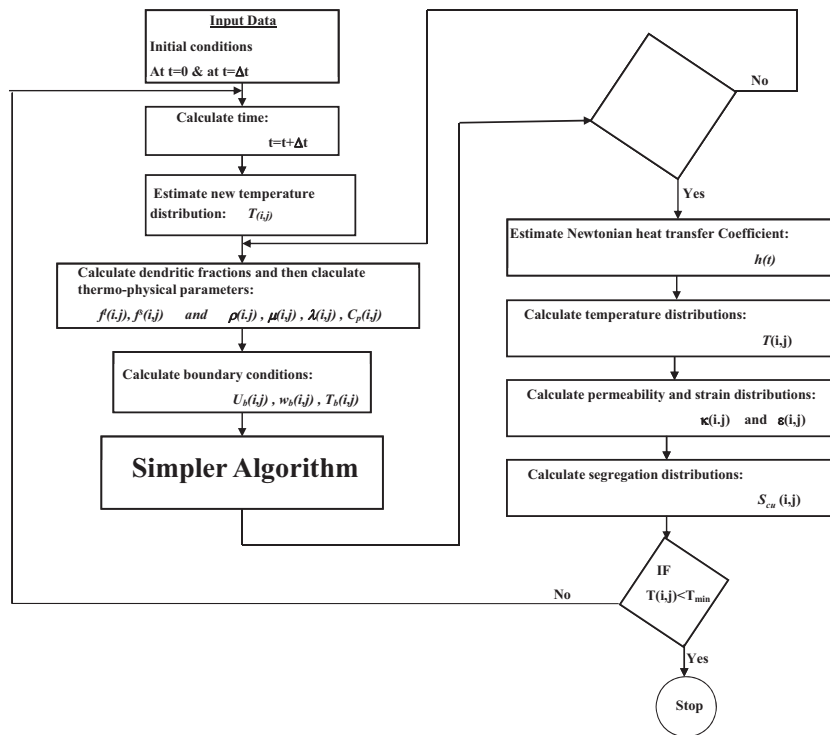**Table 4.** Equations of initial and boundary conditions.

Figure 2. Schematic illustration of simpler algorithm flow chart.

3.2. Numerical Analysis

The transformed numerical equations of governing equation in this model and illustrated in above sections are difficult to obtain them analytically and a numerical integration is available. The above partial differential equations turned into a practical scheme of computation by using the implicit finite difference simpler method proposed by Patanker.[28] Each of this method steps is discussed in more detail hereafter.

3.2.1. Numerical Analysis Details
These equations were discretized based on implicit finite difference simpler method described in Ref. [28]. This method was designed to turn the partial differential equations of convection currents problems into discretization equations where the partial derivation of equations were replaced by difference quotients by using forward implicit finite difference schemes and its grid of computation is represented in Figure 1a. The control volume of computations is shown in Figure 1b where the field is discretized into control volume elements of size $(\Delta x \times \Delta z)$ with control centers being designated by i in the x-direction and j in z direction. u Values are located at side faces of control volume element and w values are located at the side faces. Consequently, w values are at the upper and lower faces while specific parameter values such as u, w, T, ε, and S_{Cu} are located at the control volume center illustrated in Figure 1b. The derivation of each above parameters in two-dimensional form can be written in

numerical formula as follows;

$$a_{i,j}\eta_{i,j} = \sum a_{nb}\eta_{nb} + b_{i,j} \tag{1}$$

where

$$\sum a_{nb}\eta_{nb} = a_{i+1,j}\eta_{i+1,j} + a_{i-1,j}\eta_{i-1,j} + a_{i,j+1}\eta_{i,j+1} + a_{i,j-1}\eta_{i,j-1} \tag{2}$$

This numerical method and its solution for the system have been explained in detail elsewhere[28] and the symbols are defined in the nomenclature at the end of this article. These equations were solved by using a time step $\Delta t = 1\,s$. The new temperature of iteration "$n+1$" in this computation at time t in simpler method was obtained through the interpolation of old iteration "n," which was previously calculated by the same method and the calculation of new temperature, was based on the following criterion;

For time interval Δt

$$\left.\frac{\partial T}{\partial t}\right|_{n+1} \approx \left.\frac{\partial T}{\partial t}\right|_{n} \tag{3}$$

For the convergence of temperature fields, the following aspect was employed as follows;

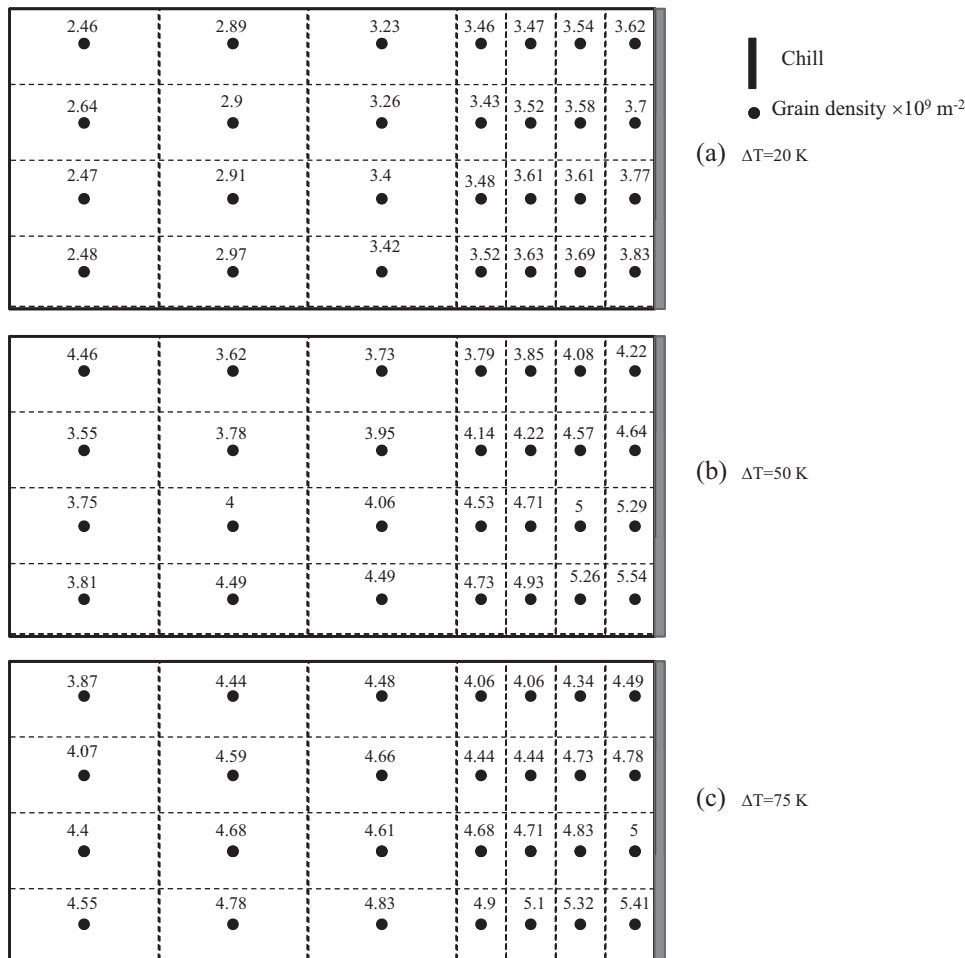$$\sum \left| \frac{T^{n+1} - T^{n}}{T^{n+1}} \right| \prec 1 \times 10^{-4} \tag{4}$$

(a) ΔT=20 K — Grain density ×10⁹ m⁻² (Chill)

2.46	2.89	3.23	3.46	3.47	3.54	3.62
2.64	2.9	3.26	3.43	3.52	3.58	3.7
2.47	2.91	3.4	3.48	3.61	3.61	3.77
2.48	2.97	3.42	3.52	3.63	3.69	3.83

(b) ΔT=50 K

4.46	3.62	3.73	3.79	3.85	4.08	4.22
3.55	3.78	3.95	4.14	4.22	4.57	4.64
3.75	4	4.06	4.53	4.71	5	5.29
3.81	4.49	4.49	4.73	4.93	5.26	5.54

(c) ΔT=75 K

3.87	4.44	4.48	4.06	4.06	4.34	4.49
4.07	4.59	4.66	4.44	4.44	4.73	4.78
4.4	4.68	4.61	4.68	4.71	4.83	5
4.55	4.78	4.83	4.9	5.1	5.32	5.41

Figure 3. Variation of grain density for different control elements of longitudinal cross section with superheats a) 20 K, b) 50 K, and c) 75 K for Al–4.5% Cu alloy.

3.2.2. Strategy Procedure

The strategy for the fully solution computation steps of heat transfer, solidification behaviors, permeability, interdendritic strain, and macrosegregation formation during dendritic solidification processes is used as follows;

(1) Read the input file.
(2) Estimate new casting temperature distribution $T(i,j)$.
(3) Calculate different dendritic solid and interdendritic liquid phase fractions ($f^i(i,j)$.
(4) Calculate thermo-physical properties of alloy $\rho(i,j)$, $\lambda(i,j)$, and so on.
(5) Calculate the convection velocity components by using simpler method.
(6) Repeat steps (2, 3, 4, and 5) until converged solutions of every quantity $I(i,j)$ are obtained.
(7) Estimate initial Newtonian heat transfer coefficient $h(t)$.
(8) Analyze thermal fields and their temperature gradients.
(9) Calculate permeability $\kappa(i,j)$, dendrite coherent "T_{coh}" and interdendritic strain distribution $\varepsilon(i,j)$.
(10) Calculate the macrosegregation distribution $S_{cu}(i,j)$.
(11) Calculate actual and new solidus temperature due to macrosegregation effect.
(12) Go to step (2) and repeat the above steps.

The major steps in this strategy involved in the solution are shown as a flow chart in **Figure 2**.

4. Numerical Results, Comparisons, and Discussion

4.1. Comparison Between Predicted and Measured Results

In this section, the segregation ratio distributions of both experimental and numerical results are compared for dendritic equiaxed solidification of Al–4.5% Cu alloy. The mushy permeability "κ" of these simulations were calculated by using the measurements of grain size presented in Figure 9a–c in Part I of this paper and the calculated grain
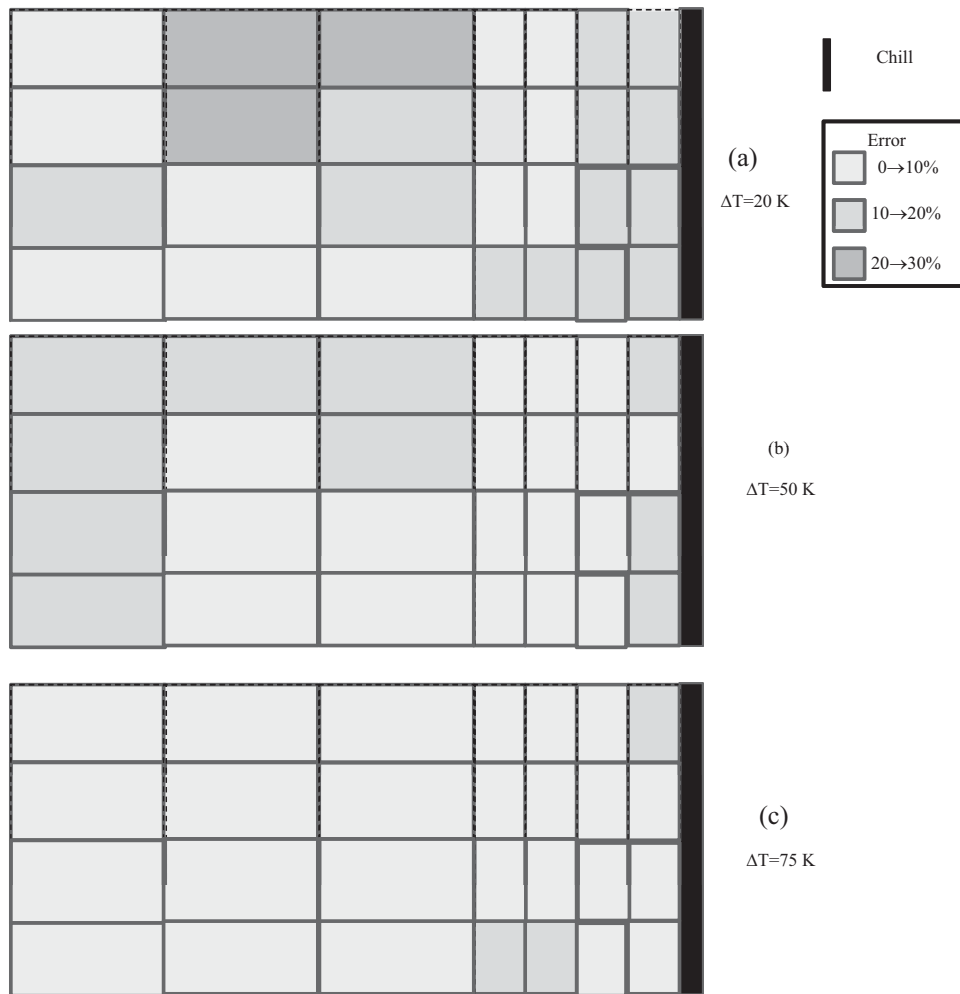
Figure 4. Variation of segregation errors with complete diffusion mechanism with superheats a) 20 K, b) 50 K and c) 75 K for Al–4.5% Cu alloy.

density distributions are shown in **Figure 3**a–c.[23,27] Comparisons are made between numerical predications and experimental data in terms of the errors in evolution of copper segregation by using the following equation:

$$E_r = \frac{S_{Cu}^P - S_{Cu}^M}{S_{Cu}^M} \times 100 \tag{5}$$

where E_r, S_{Cu}^P, and S_{Cu}^M are error percent, predicted, and measured segregations of copper, respectively. These error comparisons are shown in **Figure 4**a–c to 6a–c for complete, some ($\alpha^* = 0.25$) and no diffusion mechanisms, respectively with different superheats. These figures show different reasonable agreements based on the diffusion mechanism and the location of control volume in ingot. The observed deviations between the predications of different diffusion mechanisms are probably due to the differences between the natural diffusion mechanisms in dendritic solid. This will be discussed in the following sections. Also, these disagreements may be because the

evaluation of macrosegregation does not agree exactly the theoretical treatments and boundary conditions where these errors are also due to the lag for example in thermo-physical properties of Al–Cu alloy.

Moreover, comparisons between available cooling curves and model predications have been conducted for locations T2-bottom and T1-top, see Figure 1a. These comparisons are shown in **Figure 7**a, b and **8**a, b for 20 and 75 K superheats, respectively. These figures show that the calculated cooling curves are in the reasonable agreements with measured ones for different superheats. An interesting observation arises from this comparison where the deviation between measured and predicted cooling curve is observed particularly at location T2-bottom, with 20 K superheat, see Figure 7a. This deviation decreases with increasing the melt superheat as shown in Figure 8a. These disagreements are probably related to the assumptions used in the model and lag in detail of thermo-physical properties. In addition to these, and as already discussed in Refs.,[29,30] the model neglected the
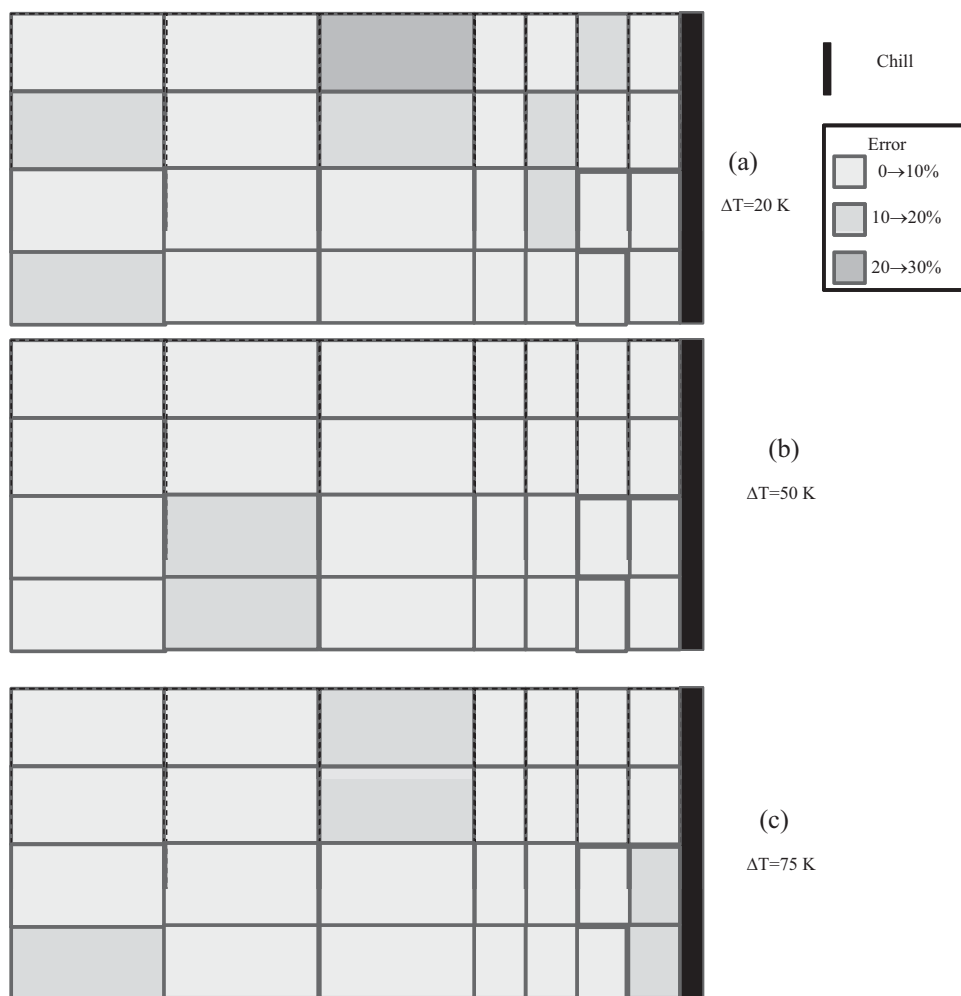
Figure 5. Variation of segregation errors with some diffusion mechanism with superheats a) 20 K, b) 50 K, and c) 75 K for Al–4.5% Cu alloy.

solute convection and the movement of free crystals due to the density difference between solid and liquid under the influence of convection streams or gravity.

In general, the predicted results indicate also that the cooling rates are slow and the cooling is continuous where there are no fluctuations observed. The measured temperature data and the model predications have been used to evaluate Newtonian heat transfer coefficient, thermal fields, dendritic solidification behavior, convection stream patterns, interdendritic strain generation, and finally macrosegregation in early stages of solidification under steady state chill cooling conditions and various melt superheats.

4.2. Heat Flow Analysis

The effect of different melt superheats on the Newtonian heat transfer coefficient ''h'' and temperature gradients

''T_G'' with time and distance from chill are illustrated in **Figure 9** through 10a–c, respectively. Also, the heat flow analysis of Newtonian heat transfer coefficient appears the various cooling regions of air gap formation as well as the effect of different superheats on these cooling regions. Moreover, this analysis shows the effect of various cooling regions on the thermal fields represented as temperature gradients during the dendritic equiaxed solidification.

4.2.1. Newtonian Heat Transfer Coefficient ''h''
Figure 9 shows the variation of Newtonian heat transfer coefficient ''h'' as function of time with different melt superheats. Overall, it can be seen from Figure 9 that the heat transfer coefficient has the same trend in various cooling regions. Figure 9 also, indicates generally that the higher superheat is accompanied by higher heat transfer coefficient during various cooling regions of air gap. These results agree quantitatively and qualitatively well with the observations and predications of El-Mahallawy and Assar[31] and might help to explain various heat transfer
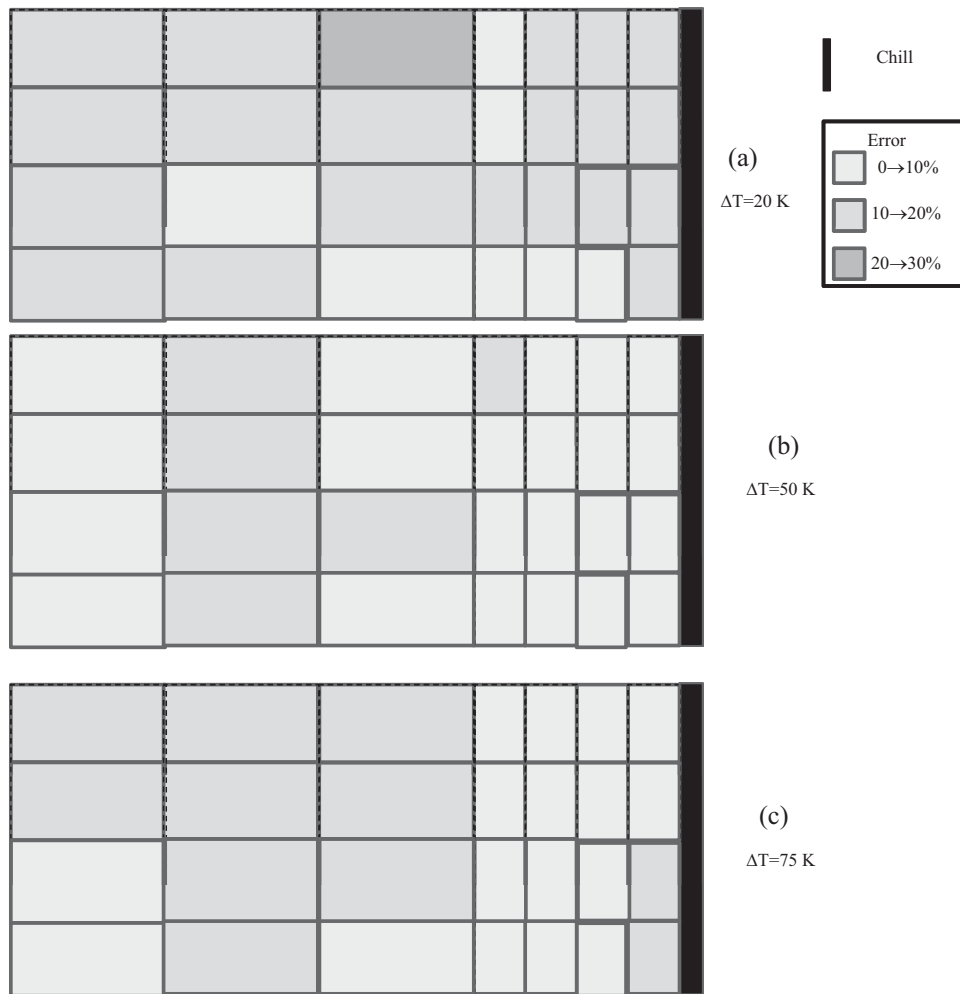
Figure 6. Variation of segregation errors with no diffusion mechanism with superheats a) 20 K, b) 50 K, and c) 75 K for Al–4.5% Cu alloy.

phenomena associated with cooling of poured liquid metal. Referring to Refs.[3] through,[32,33] the cooling conditions in chill ingot casting can be classified into two main regions. The first region covers the region of before air gap formation ''BAGF'' whereas the second one is the region of after air gap formation ''AAGF'' as shown in Figure 9. Every cooling region consists of several sub-regions. In these sub-regions, the cooling conditions behave in different ways based on the heat transfer mode controlled by the natural of cooling and solidification processes.

At pouring temperature, it is considered that heat transfer controlled by natural convection streams in liquid region where the heat transfer phenomenon depends on the type of convection. Therefore, the initial value ''h'' in this sub-region of BAGF region is always low values. The values take approximately, 150, 200, and 250 W m^{-2} K^{-1} for 20, 50, and 75 K superheats, respectively. Consequently, these values increase slightly by different small rates based on the superheat magnitude. Therefore, these values depend on the magnitude and direction of natural con-

vection velocities until the liquidus temperature. As solidification starts, the interdendritic mushy incoherent region initiates and dendritic solid begins to grow. Due to the formation of dendritic solid, the heat transfer mode changes[34] and h increases by higher rates than the liquid region. As solidification continues, the dendritic solid grows in the mushy zone and h increases slowly based on the type of solidification mode until the coherent temperature. At the initial of interdendritic mushy coherent region, it obvious that h rises rapidly from initial contact values of 390, 1200, and 1800 W m^{-2} K^{-1} until peak values 1150, 4650, and 10400 W m^{-2} K^{-1} for 20, 50, and 75 K superheats, respectively. The rise in h from an initial low value to a peak value is well established[34–37] but the mechanism by which this occurs and the time interval of its occurrence, is not well understood. This is due the natural of dendrite coherent phenomena[15] depending on the alloy system, structure and experimental set up.[31,35–37] Recently, El-Bealy and Hammouda[34] proposed the mechanism explained this phenomenon and its effect on chill
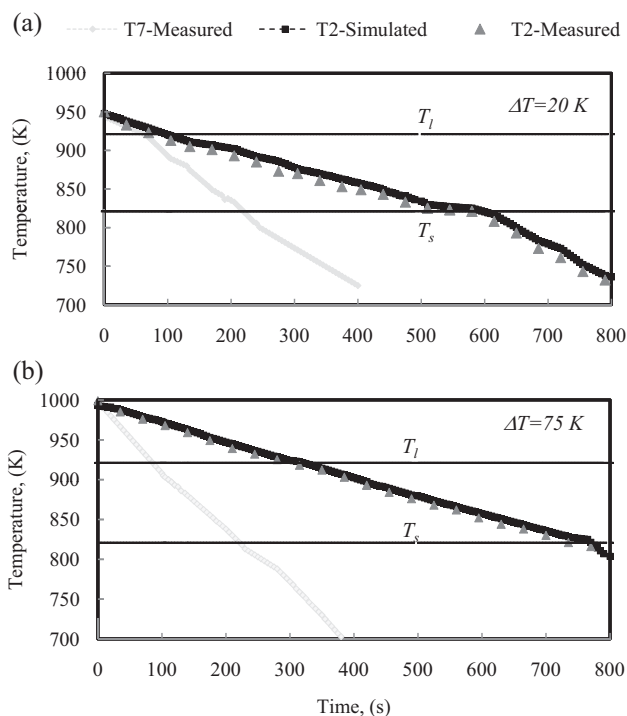
(a)

(b)

(a)

(b)

Figure 7. Comparing between experimental and simulated cooling curves with superheats a) 20 and b) 75 K at position T2 for Al–4.5% Cu alloy.

Figure 8. Comparing between experimental and simulated cooling curves with superheats a) 20 and b) K 75 at position T1 for Al–4.5% Cu alloy.

zone formation. They pointed out that the type of heat flow mode changes from convection to conduction mode. This is due to change in the contact type of chill/ingot interface and its area where the mushy coherent phenomenon plays a major role to define this mechanism. This results in an increase in the temperature gradient "G" in the mushy zone and changing in the type and magnitude of interdendritic strain generation.

Once the solidifying shell becomes self-supporting, it contracts in accordance with thermo-mechanical and shrinkage properties of casting, while the chill surface may expand. The relative magnitude of the casting contract, shrinkage, and the chill expansion, together with any pressure acting on the interface determines the contact type of the chill/ingot interface and therefore controls the heat transfer coefficient in the after air gap formation region "AAGF." Subsequently, the peak values decline sharply to 690, 1200, and 2000 W m^{-2} K^{-1} for 20, 50, and 75 K superheats, respectively. This sub-region can be defined as after air gap-separated sub-region "AAG$_{sp}$." This is due to initial sub-region of air gap formation which the solidifying shell separates completely or partially from chill and therefore, there is no or small contact between them. This results in a sharp increase in the thermal resistance of chill/ingot interface and therefore, a steep decrease in the interfacial heat flux.[38,39] This mechanism has been confirmed by Ho and Pehlke[38] who used transducers to sense interface movement and a circuit to monitor elec-
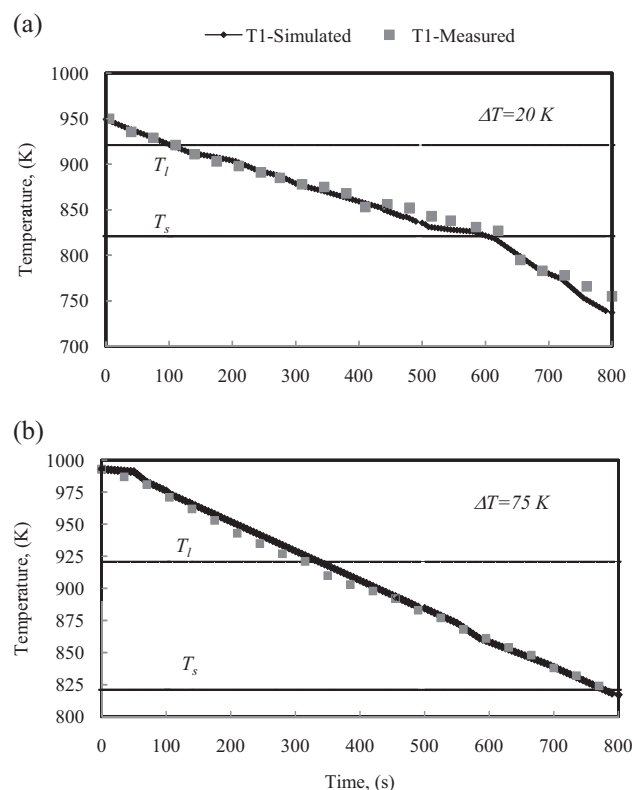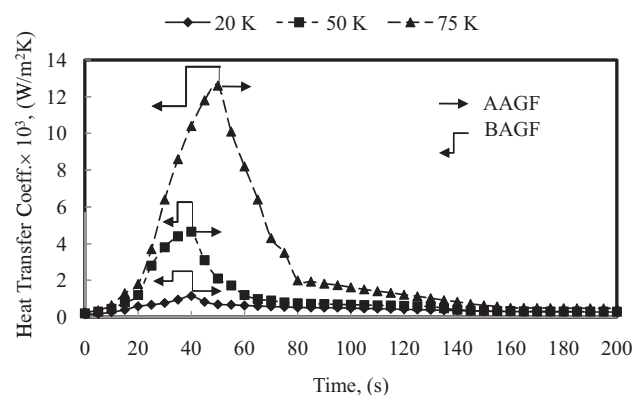

Figure 9. Variation of Newtonian heat transfer coefficient "h" with different superheats.

trical continuity between chill and casting. They found that the electrical circuit breaks down at the onset of a sudden drop in interfacial heat transfer. A further drop in interfacial heat flux occurs as the width of gap grows, coupled with increasing thermal resistance of solidified shell which results in a small decrease in h with time until values 517, 590, 640 W m^{-2} K^{-1} for 20, 50, and 75 K superheats, respectively. This sub-region may be called after air gap-growth
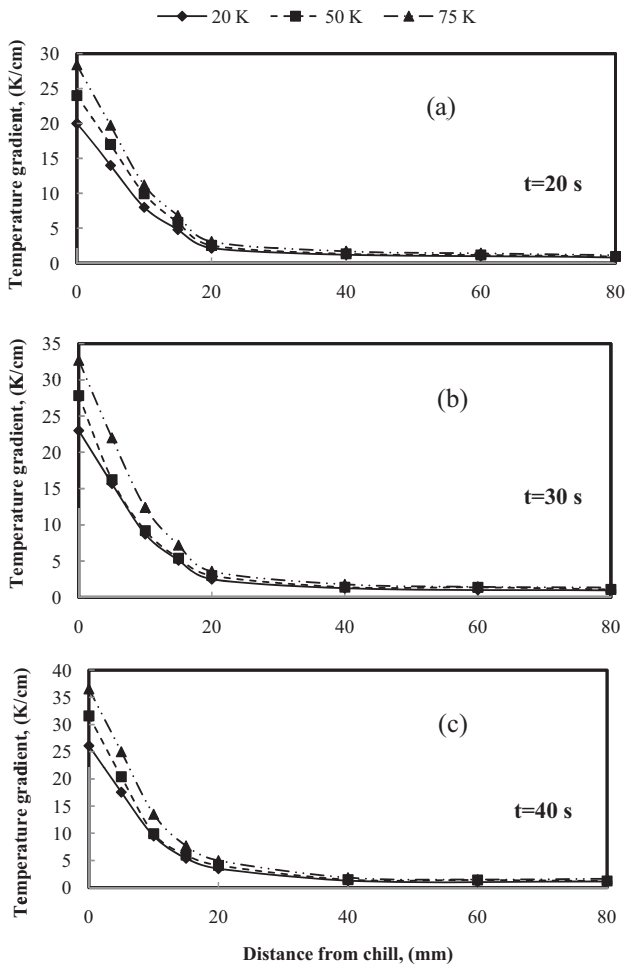
Figure 10. Variation of temperature gradients with superheats a) 20 K, b) 50 K, and c) 75 K as function of distance from chill at different times for Al–4.5% Cu alloy.
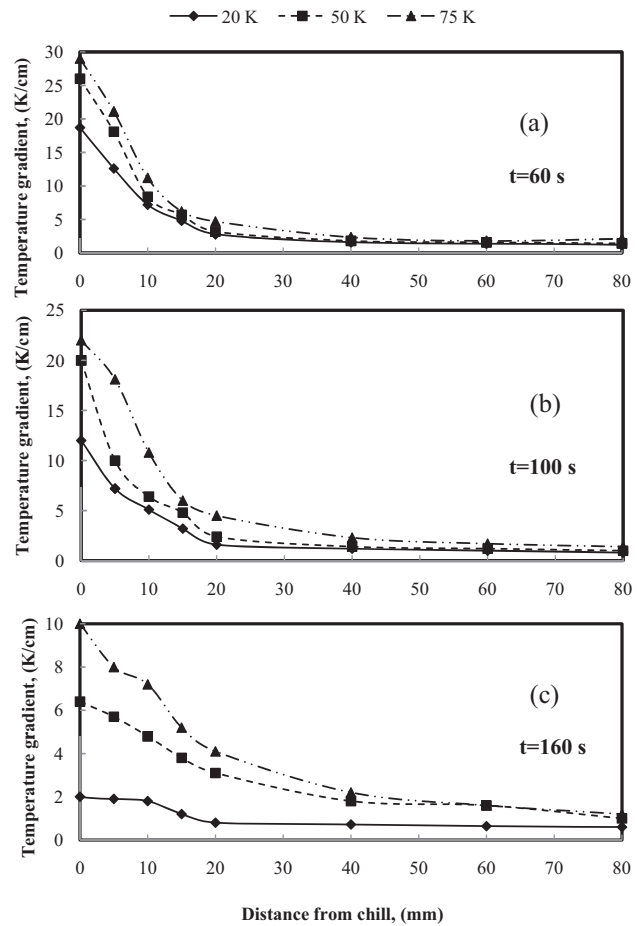

Figure 11. Variation of temperature gradients with superheats a) 20 K, b) 50 K, and c) 75 K as function of distance from chill at different times for Al–4.5% Cu alloy.

sub-region "AAG$_g$." From the onset of a steadily growing gap, the air gap increases very slowly which results in a very slight decrease in h until values of 280, 293, and 473 W m^{-2} K^{-1} at time of 200 s as shown in Figure 9 for 20, 50, and 75 K superheats, respectively. This sub-region may defined as after air gap-steady state sub-region "AAG$_{st}$" where in this sub-region, other factors such as the shrinkage characteristics of the casting, the expansion characteristics of the chill, the thermal diffusivity of the gap and the solidifying shell and the surface oxidation characteristics of the chill and casting become dominant in controlling heat transfer phenomenon.

4.2.2. Temperature Gradients "G"

It has been suggested that the heat transfer characteristics of solidified alloy help much to explain the mechanisms of transport phenomena, interdendritic strain generation and therefore, casting defects associated with dendritic solidification processes. Therefore, the temperature gradient "G" in the mushy zone has been recorded during the

calculations in various cooling regions with different melt superheats. The average values of G are plotted in Figure 10a–c and 11a–c as a function of distance from chill at different times represented the sub-regions of before air gap and after air gap formation regions. The predicted results indicate that the temperature gradient has the same distribution profile with different superheats and it varies with distance from chill.

In the case of before air gap cooling region, Figure 10a–c illustrates the temperature gradients with distance from chill at various times and locations with different superheats. The model results show the same trend with different casting conditions where G is high at ingot surface and reduces gradually to the small values at 20 mm followed by slight decreasing in G until 80 mm from chill. These values increase with time during this cooling region especially at chill ($x = 0$) and within the first 20 mm from chill for different superheats. The differences in G values with different superheats are observed particularly at chill ($x = 0$). These differences reduce and convene with distance until small values at 20 mm. Subsequently, these differences decrease
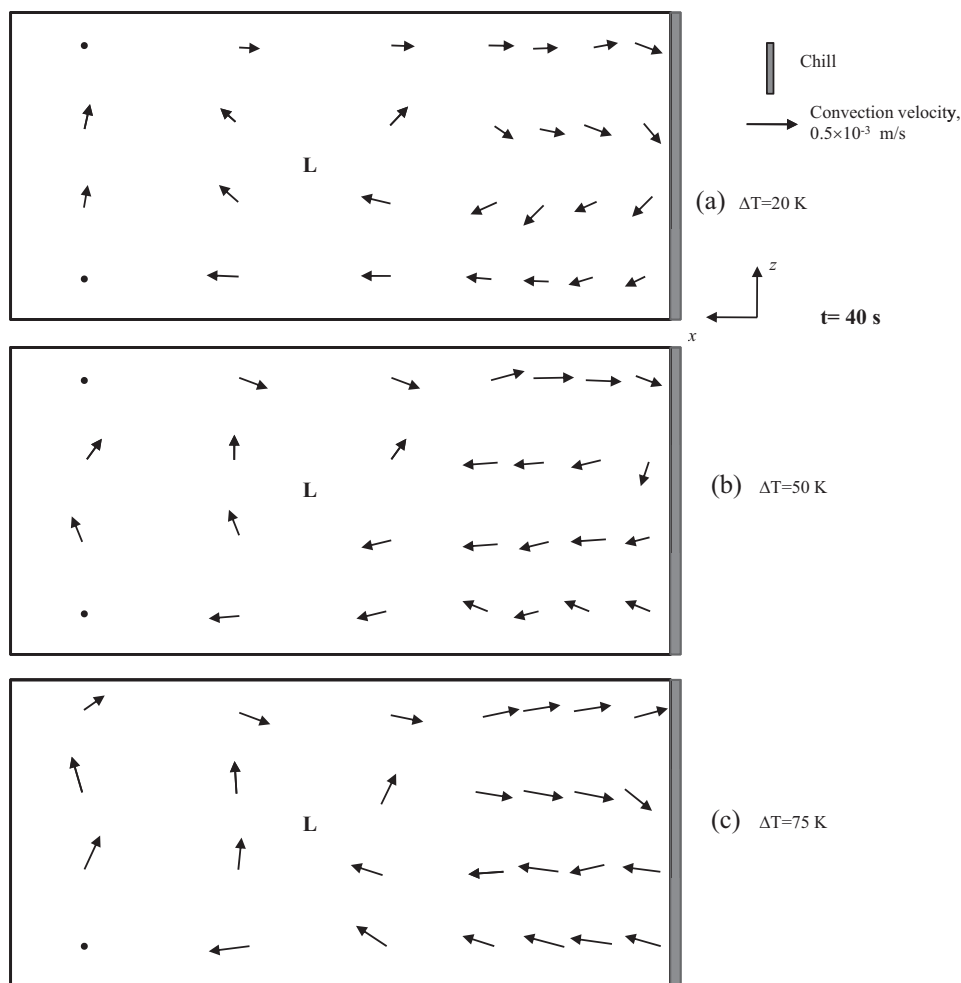
Figure 12. Simulated convection velocity pattern at $t = 40$ s with superheats a) 20 K, b) 50 K, and c) 75 K for Al–4.5% Cu alloy.

continuously until very small values at 80 mm from chill. This mechanism of G profiles agrees well with the predications of El-Bealy and Fredriksson[8,39] and might explain and complete his explanation why interdendritic midface longitudinal cracks of continuously cast peritectic steels slabs associated with steep surface segregation. From another side, it might describe the mechanism behind the extruded surface segregation layer and why this phenomenon is always found in aluminum direct chill ingots by different degrees.[33] These phenomena depend on the behavior of rising mechanism in heat transfer coefficient "h" from initial small value to a peak value seen in Figure 9. This mechanism is well established[33,39] but the mechanism by which this occurs and the time interval of its occurrence is not well understood. The time to attain the peak value of h has been reported to vary from low values of less than a second to high values of more than 30 s, depending on the alloy system and experimental set up.[35–37] These results of time interval agree well with the present results where the time intervals vary from 40, 42, and 45 s for 20, 50, and 75 K superheats, respectively.

As solidification progresses, the air gap begins to form. **Figure 11**a–c depicts the temperature gradient "G" at time of 60, 100, 160 s, respectively, with different superheats and locations from chill. These figures show the reduction in G in the surface and sub-surface areas close to chill until 20 mm whereas the rest of locations until 80 mm in which G increases slightly as shown in Figure 11a–c. Generally, the values of surface and subsurface temperature gradients until 20 mm from chill decrease continuously from $t = 60$ s into $t = 160$ s by different ratios. The total surface ratios at $x = 0$ change from 65, 23, to 89% for 20, 50, and 75 K superheats, respectively. The results show also that the difference between G of different superheats increases for all locations with time in this cooling region. Also, these ratios change by different ratios with different locations in cast ingot as shown in Figure 11a–c. These predications of reduction in G agree well with most of the findings and predicted hypotheses of previous researchers[14,40,41] and might explain and complete their explanations[42–43] why surface and subsurface interdendritic cracks are associated with the reduction in the surface cooling due to air gap
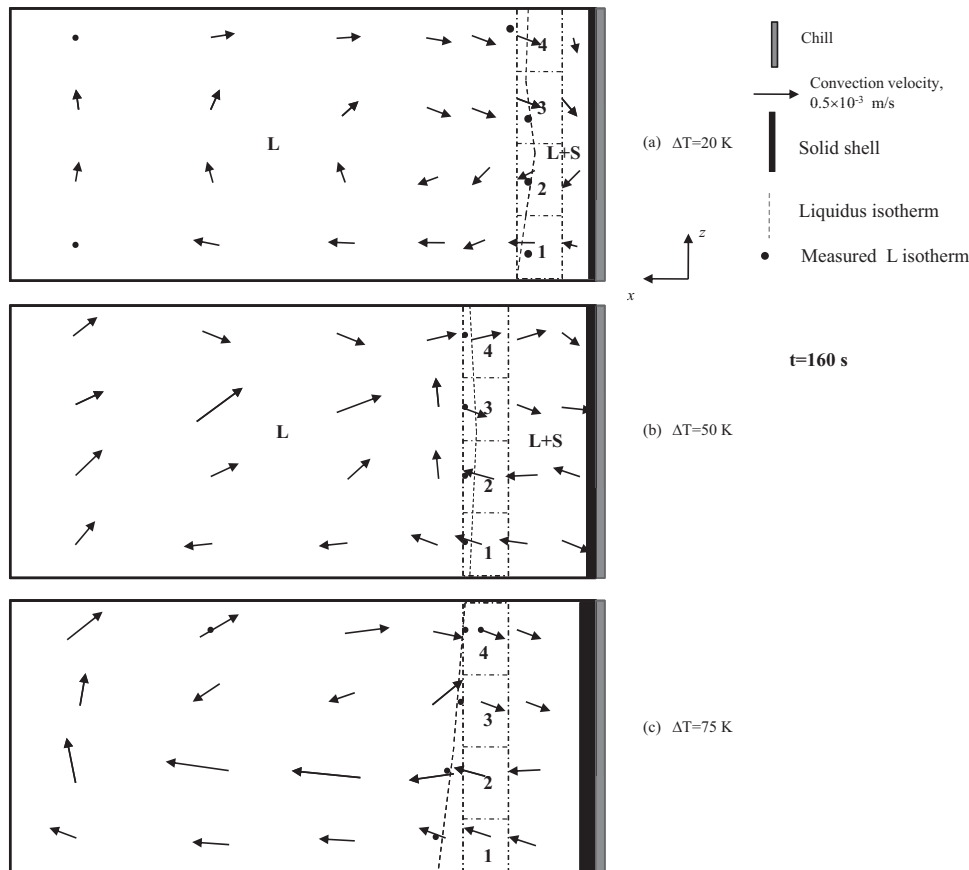
Figure 13. Simulated convection velocity pattern at $t = 160$ s with superheats a) 20 K, b) 50 K, and c) 75 K for Al–4.5% Cu alloy.

formation and its propagation. This results in a steep reduction in the surface temperature gradient and therefore accumulates the high interdendritic strain in the interdendritic areas close to solidus isotherm.[8] Consequently, this reduction mechanism in heat transfer coefficient ''h'' is due to the air gap formation and its width propagation. This results in a steep reduction of h from a peak value to a small value seen in Figure 9. This reduction has a complete responsibility to form a steep interdendritic tensile strain and therefore rapid changing in the interdendritic rich solute liquid followed by increasing in the width of mushy coherent region cracks which result in initiation and growth of interdendritic sub-surface cracks. This mechanism is well published[8,10,44,45] but the mechanism by which this occurs and the time interval of its occurrence is not well understood due to unclear and complex of natural and behavior of air gap formation.[14,46]

4.3. Melt Convection and Mushy Permeability Analysis

The thermal convection stream patterns or mushy permeability are often used as criteria for the formation of macrosegregation during dendritic solidification.[34,47–49]

The results of three simulations of the thermal convection stream patterns are presented here in **Figure 12**a–c to **14**a–c whereas the grain density distributions which use to calculate the mushy permeability are shown in Figure 3a–c for 20, 50, and 75 K superheats, respectively. The comparisons revealed in **Figure 13**a–c and 14a–c between the measured liquidus isotherms from cooling curves and simulated results show good agreements.

4.3.1. Melt Convection Streams
At early stage of cooling process ($t = 40$ s), the flow field of liquid phase, see Figure 12a–c, consists of a single clockwise rotating convection cell with all superheats. This liquid flow is only driven by thermal convection but the effect of sedimentation of the forming separated free crystals from chill wall into melt liquid is observed, see Figure 3a–c. In addition to change in density of liquid melt due to the cooling, the downward flow of the separated free crystal from chill due to its higher density than the liquid exerts a large interfacial drag on the liquid and pulls the liquid downward. This sedimentation driven liquid further augments the thermal buoyancy forces in the liquid shown in Figure 12a. Convection driven by sedimentation has been researched little and deserves more attention where it was ignored in this study. Evidence for this phenomenon,
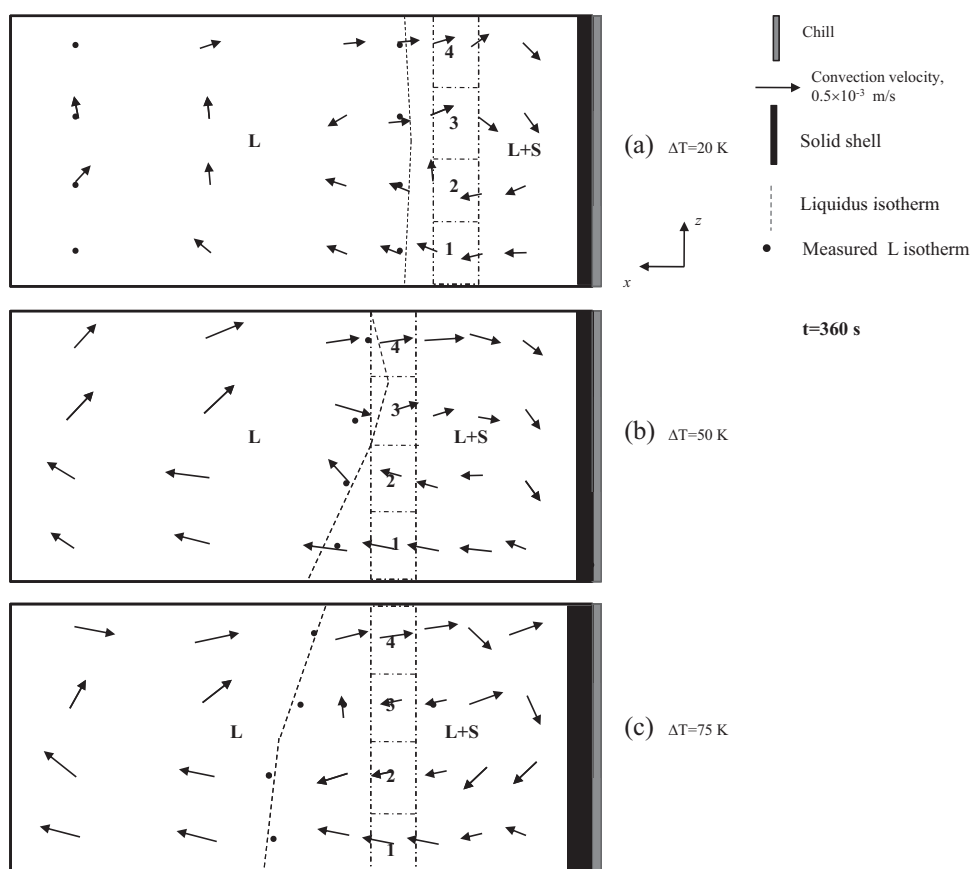
Figure 14. Simulated convection velocity pattern at $t = 360$ s with superheats a) 20 K, b) 50 K, and c) 75 K for Al–4.5% Cu alloy.

it can be seen in the direction of sedimentation of equiaxed crystals as shown in micrographs 6(a,b), 7(a,b), and 8(a,b) of Part I for this two part papers. These micrographs show that random direction of sedimentation of equiaxed crystals on the surface as illustrated in micrographs 6(a), 7(a), and 8(a). This is due to different directions of surface convection streams as shown in Figure 12a–c. However, the direction of sedimentation of equiaxed crystals in the interior areas at ingot bottom is one direction parallel to ingot bottom as shown in micrographs 6(b), 7(b), and 8(b) in Part I of this paper. This results from the nature and direction of convection streams direction of bottom interior areas illustrated in Figure 12a–c and may generate slight differences of directions of sedimentation of equiaxed crystals in the interior areas.

The convection streams shown in Figure 12a–c indicate that some separated crystals that nucleated and grew along the chill wall may be swept by the liquid flow into the superheated middle region elements of cast ingot. This agrees well with the grain density distributions in these elements, see Figure 3a–c, and their convection streams directions shown in Figure 12a–c. Also, the grain density plots shown in Figure 3a–c illustrate the another trend, since higher grain density associated with sedimentation mechanism appears in the first bottom rows of ingot

whereas the small change in the grain density distribution probably associated with sweeping the free crystals is visible in the same rows. This agrees well with the observations and predications by El-Bealy and Hammouda[34] and might explain the mechanism of the effect of convection streams on the crystal separation and free crystals with dendritic equiaxed structure formation and its growth.

At early stage of solidification ($t = 160$ s), results shown in Figure 13a–c illustrated that an mushy zone forming with irregular liquidus isotherm and thin solid shell appeared on the ingot surface which appeared as black area close to the surface. The convection stream patterns shown in Figure 13a–c follow the same trend where these patterns in liquid zone and are mostly upward, particularly in the hotter regions in left hand side of ingot. These patterns show an interesting feature of liquidus isotherms where these isotherms are not straight and the bottom parts always cooler than upper parts. This is due to the effect of the direction of convection streams where these streams transfer the heat from bottom regions into upper regions close to liquidus isotherm as shown in Figure 13a–c. Because of a high solidification rate of the sedimenting crystals, a significant amount of latent heat is released in the lower portion controlling the extended of liquidus isotherm in this portion.[30,49] This agree well with com-

parisons the grain densities in upper portion to those in the lower one where the differences are not high. Another interesting phenomenon arises from these results where all solidus isotherms are straight, thin, and the solid shell thicknesses are 1.3, 2.1, and 3.2 mm for 20, 50, and 75 K superheats, respectively. The straightness in these isotherms are due to wide mushy zone for this alloy system where the solidification interval is equal to 100 K and also due to small quantities of convection velocities.

Simulations results at an intermediate stage of solidification ($t = 360$ s) are shown in Figure 14a–c for different superheats. These plots show that the convection stream patterns still keep the same trend. But, it is observed that there is a small and weak rotating convection clockwise cell seen inside the mushy zones in the middle regions. Also, the figures show that only a thin solid shell exists in the right hand side along the chill with thickness 2.9, 3.7, and 5.3 mm for 20, 50, and 75 K superheats, respectively. However, in the left hand side of ingot, a large pure liquid zone can be observed. Between two zones, wide mushy zone appears with irregular liquidus isotherm for all cases. Due to significant convection streams at this stage of solidification, the mushy zone remains somewhat wider in the bottom portions than the upper portions. Subsequently, the mechanism of sedimentation of crystals is significant to occur especially with higher superheats.[30,49] The grain density distributions shown in Figure 3b and c agree well this phenomenon where significant differences in grain density are observed.

4.3.2. Grain Density Distribution

The nature of the equiaxed crystal structure evolving during dendritic solidification processes can be deduced from 3(a–c) for different superheats. Consequently, the grain density is another interesting microstructure parameter controlled dendrite mushy permeability phenomenon. The grain density distributions calculated from the measurements of grain size in the Part I of this two parts paper. The local grain density is not only determined by nucleation rate and its growth rate but it is also influence by the solid motion during solidification.[30,34,49] The advection of solid will cause a redistribution of the grains and nuclei, in addition to influencing the nucleation and growth processes themselves. El-Bealy and Hammouda[34] proposed a simple approach called control volume technique ''CV'' which is based on a small control volume controlled by the net flow of out and inter convection streams shown in Figure 1b.

In the early stage of solidification ($t = 160$ s), Figure 13a–c show mushy control volume elements from CV1 to CV4 as well as convection stream patterns for superheats 20, 50, and 75 K, respectively. At superheat 20 K, see Figure 13a, the velocities at all position were predicted is very small within numerical accuracy. Consequently, the ingot system is approximately convectively stable and convection velocities are insufficient to affect the crystal movements. This agrees well with the grain density distributions in

different control volume elements shown in **Figure 15**a where the change in the grain density is very small and is within 4.1% between CV1 in the ingot bottom and CV4 in the ingot top (column no. 2). This is due to small number of heavy separated crystals which results in a low number of free crystals and may float in the bulk liquid.[48,50] For this reason, the number of sedimentation crystals increases slightly in ingot bottom volume CV1 than top one CV4 where the direction of velocities in bottom volume CV1 helps the low density free crystals to float again into hotter regions in mushy region or in liquid zone as shown in Figure 13a.[30,34,49] In the second ingot at 50 K superheat, Figure 13b shows that there is an observed change in grain density distributions of maximum change 22.4% between CV1 in the ingot bottom and CV4 in the ingot top. This is due to increase the number of separated crystals from chill wall which have low densities.[48,50] The low density free crystals may have a higher possibility to float into liquid zone and grow in the cooler parts in bottom ingot. In addition to low convection velocities and their directions, these may have possibility to affect the movement of free crystals. This helps the mechanism of settling of these crystals close the bottom volume CV1 to increase its grain density. The mechanism of sedimentation crystals and convection stream pattern continuous upwards. Thus, the grain density decreases from CV1 into CV4 by different and particular changing rates until maximum value at CV4 as shown in Figure 13b. In the third ingot at 75 K superheat, the results shown in Figure 13c illustrate a new phenomenon associated with small, low density, and large number of separated crystals due to sufficient thermal convection streams where the free crystals float from bottom to top ingot. This results in a decreasing in the grain density and changing the ratio between CV1 in the ingot bottom and CV4 in the ingot top into maximum value of 18.4% compared to second case. This is because of decreasing in the number of settling free crystals due to the nature, magnitude, and direction of convection streams shown in Figure 13c.

As a solidification continuous and at intermediate stage of solidification ($t = 360$ s), representative results are shown in Figure 14a–c which indicate the same trend as first case of grain density distributions with different convection streams patterns of different superheats. In the first ingot at 20 K superheat, Figure 3a shows the same changing in the ratio of grain density between CV1 in the ingot bottom and CV4 in the ingot top (column no. 3) as the case of early stages of solidification (column no. 2). This is because insufficient convection streams and wide mushy zone provide more possibility of free crystals to grow and sediment in bottom control volume CV1, see Figure 14a. In the second ingot at 50 K superheat, Figure 3b illustrates that the changing ratio between CV1 and CV4 (column no. 4) reaches 19.9% for the same reasons whereas in the case of third ingot at 75 K superheat, the predicted results shown in Figure 3c indicate that the changing ratio is approximates 17.1%. This is due to the difference in con-
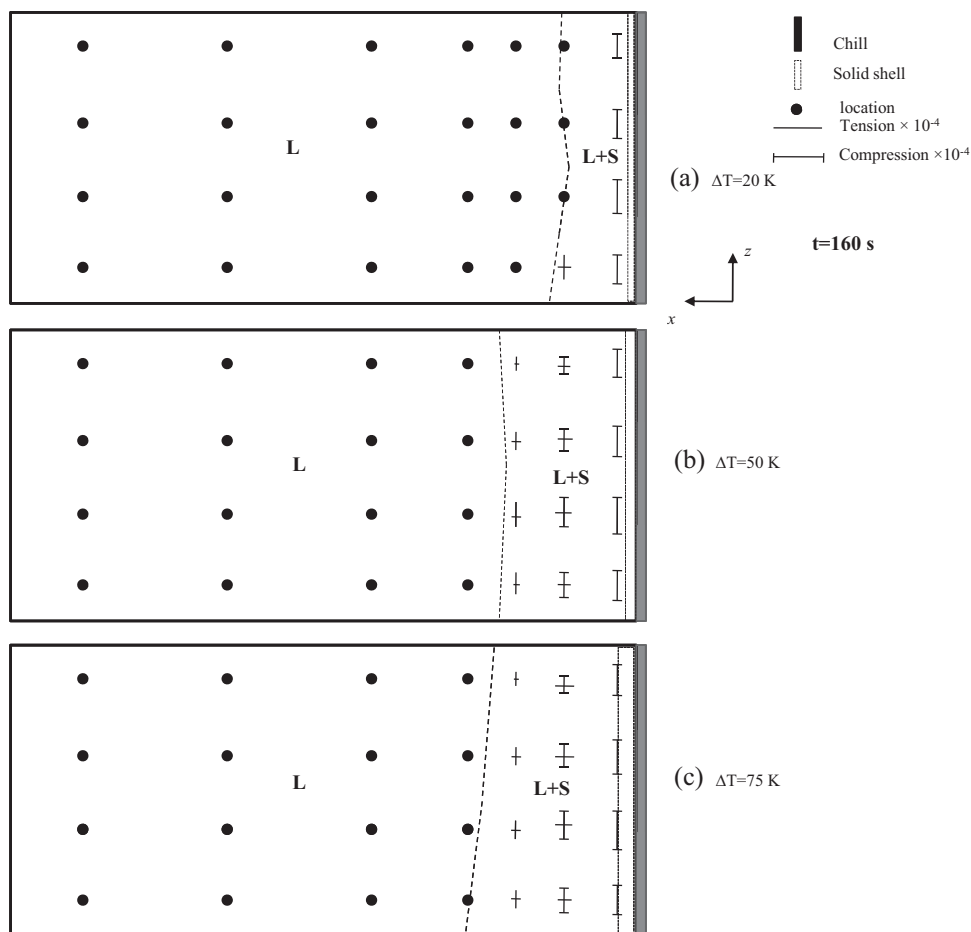
Figure 15. Simulated interdendritic strain distribution at $t = 160$ s with superheats a) 20 K, b) 50 K, and c) 75 K for Al–4.5% Cu alloy.

vection streams and in mushy zone widths of higher superheats. In general, both the mechanism of nucleation and growth of equiaxed dendritic crystals as well as the thermal convection streams of solidified alloy affect the grain density distributions, the mushy permeability and therefore the macrosegregation distributions.

4.4. Interdendritic Strain Analysis

Interdendritic strain is also often used as criteria for simulating the formation of macrosegregation.[8–10,33] Using the thermo-physical and metallurgical data for aluminum 4.5% Cu alloy, the interdendritic strain model was run to predict strain based on the temperature calculations and solidification behavior for the processing of the 80 mm × 40 mm ingots just discussed. The distributions of this criterion at each node of ingot transverse cross section in the mushy incoherent, coherent, and solid zones of ingot are plotted in Figure 15a–c and 16a–c for two different times at $t = 160$ s and $t = 360$ s, respectively, and with different superheats.

The importance of nature of mushy zone phenomena in the development of the interdendritic strain can be more clearly seen through the simultaneous examinations of Figure 15a–c and **16**b, c. These figures show that the mushy zone can be classified as two main regions. The first region is bounded by the liquidus isotherm and coherent isotherm. This region is defined as mushy incoherent region "MI$_c$R" and the interdendritic strain controlled only by shrinkage of interdendritic liquid and contraction of dendritic solid. The nature of interdendritic strain is compressed but the distance between the dendrites increases or the interdendritic area between the equiaxed crystals enlarges.[8,10] Therefore, the type of this strain should be treated it as interdendritic tensile strain.[51] This agrees well with Flemings and Nereo[2] theory of inverse segregation and explains clearly the mechanism of surface segregation shown in Figure 4a–c through 6a–c.[14] The second mushy region is defined as mushy coherent region "MCR" bounded by coherent isotherm and solidus front. In this region, the control volume element "CV" included the equiaxed crystals treats as one unit. This means that the compressive strain compresses the control volume and reduces the segregation
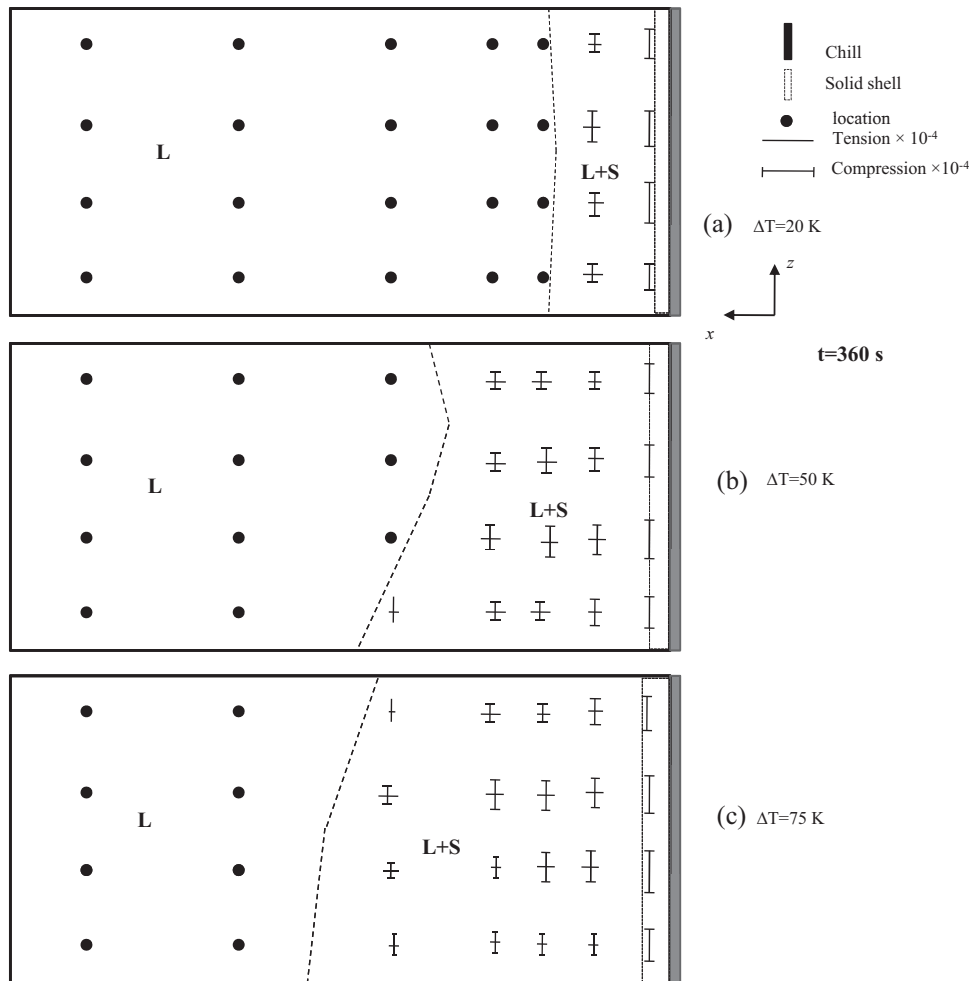
Figure 16. Simulated interdendritic strain distribution at $t = 360\,s$ with superheats a) 20 K, b) 50 K, and c) 75 K for Al–4.5% Cu alloy.

whereas the tensile strain tenses the control volume and raises the segregation.[8–10]

Figure 15a–c represents the pattern of interdendritic strain distribution that develops within the mushy zone of cast ingot by the time 160 s for 20, 50, and 75 K superheats, respectively. The model results show that the same trend for all the cast ingots where the strain pattern reveals low average interdendritic strain components in different nodes in the ingot exterior and interior within the mushy zone. The maximum values of compressive strain z–z components generated in ingot exterior are 0.7×10^{-4}, 0.76×10^{-4}, and 0.8×10^{-4} ($x = 5\,mm$) for 20, 50, and 75 K superheats, respectively. These compressive strain z–z components reduce gradually from the ingot exterior of 0.61×10^{-4} and 0.58×10^{-4} for 50 and 75 K superheats. The coherent interior nodes in MCR reveal extremely low tensile strain only in x–x direction for all the cast ingots whereas in mushy interior nodes in MI_cR expose low tensile strain in both x and z directions. The z–z components are always higher than the x–x components in MI_cR as shown in Figure 15a–c. These distributions coincide well

with the observations and predications of El-Bealy in Ref. [14] and in the experimental work in the Part I in this paper. The micrographs 11(a,b) through 13(a,b) in the Part I of this paper show rich copper spots on the equiaxed crystals due to sudden compressive strain in exterior areas as seen in Figure 11a, 12a, and 13a, for 20, 50, and 75 K, respectively. In interior areas, the interdendritic strain squeezes the rich solute liquid through very narrow interdendritic channels in the final stages of solidification and these areas appear as very small fluidity rich copper areas as shown in Figure 11b, 12b, and 13b. Therefore, this mechanism recurs in the interior areas with different morphology of rich solute interdendritic liquid between the equiaxed crystals.

Figure 16a–c present the development of interdendritic strain distributions of the exterior and interior nodes in the solid and mushy zones by the time 360 s for 20, 50, and 75 K, respectively. These figures exhibit essentially the same features as Figure 15a–c expect that solid nodes in Figure 16b and c appear higher compressive strain than mushy nodes due to high shrinkage and contraction
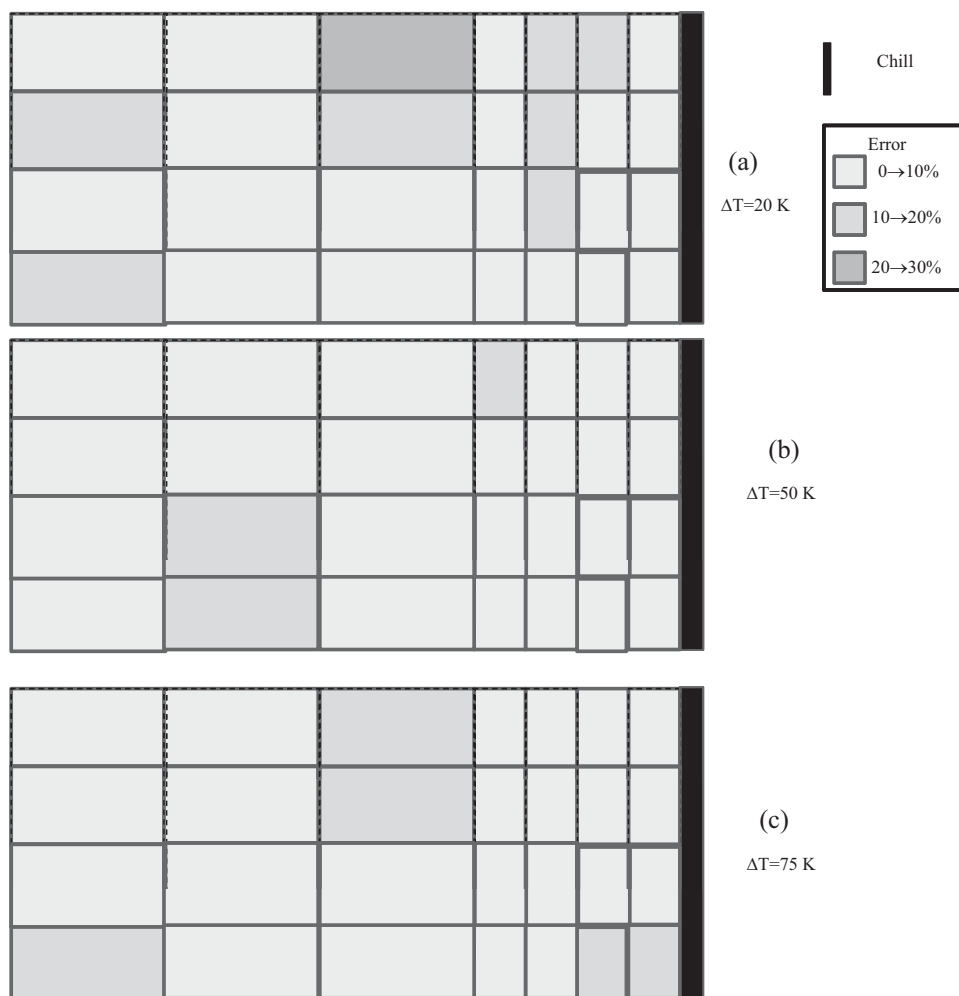
Figure 17. Variation of segregation errors with some diffusion mechanism without mushy permeability for superheats a) 20 K, b) 50 K, and c) 75 K for Al–4.5% Cu alloy.

associated with solidification and cooling of aluminum alloy in the solid zone and mushy coherent region. This might result in surface cold cracks formation shown in Figure 12a and 13a in the Part I of this two part paper. Also, the tensile strain in both x–x and z–z directions associated with the shrinkage and contraction in mushy incoherent region close to the liquidus isotherm is very clear in this case especially with 50 and 75 K superheats. Another interesting observation arises from examination of no straight liquidus isotherm in Figure 16b where bottom node appears in mushy incoherent region whereas the intermediate and top nodes reveal still in liquidus zone.

4.5. Macrosegregation Analysis

The different effects of diffusion mechanisms in dendritic solid, mushy permeability and interdendritic strain are shown in Figure 4a–c to 6a–c, and 17a–c through Figure 18a–c, respectively. Also, these figures essentially illustrate the influence of melt superheats of 20, 50, and 75 K on the macrosegregation distribution. The macro-segregation distributions of exterior and interior nodes are included in these figures as terms of segregation errors illustrated in Equation 5.

The predicted results shown in Figure 4a–c through Figure 6a–c reveal the different effects of complete diffusion, some diffusion and no diffusion mechanisms on the macro-segregation distributions, respectively, with 20, 50, and 75 K superheats, respectively. In general, different diffusion mechanisms produce dissimilar macrosegregation errors in exterior and interior nodes and these errors decrease with increasing melt superheat. The model predications in these figures show that there are random and observed differences in the segregation error values between the exterior and interior nodes especially in cases of complete and no diffusion mechanisms. This is due to different convection stream patterns. Also, various solidification, interdendritic strain and mushy permeability
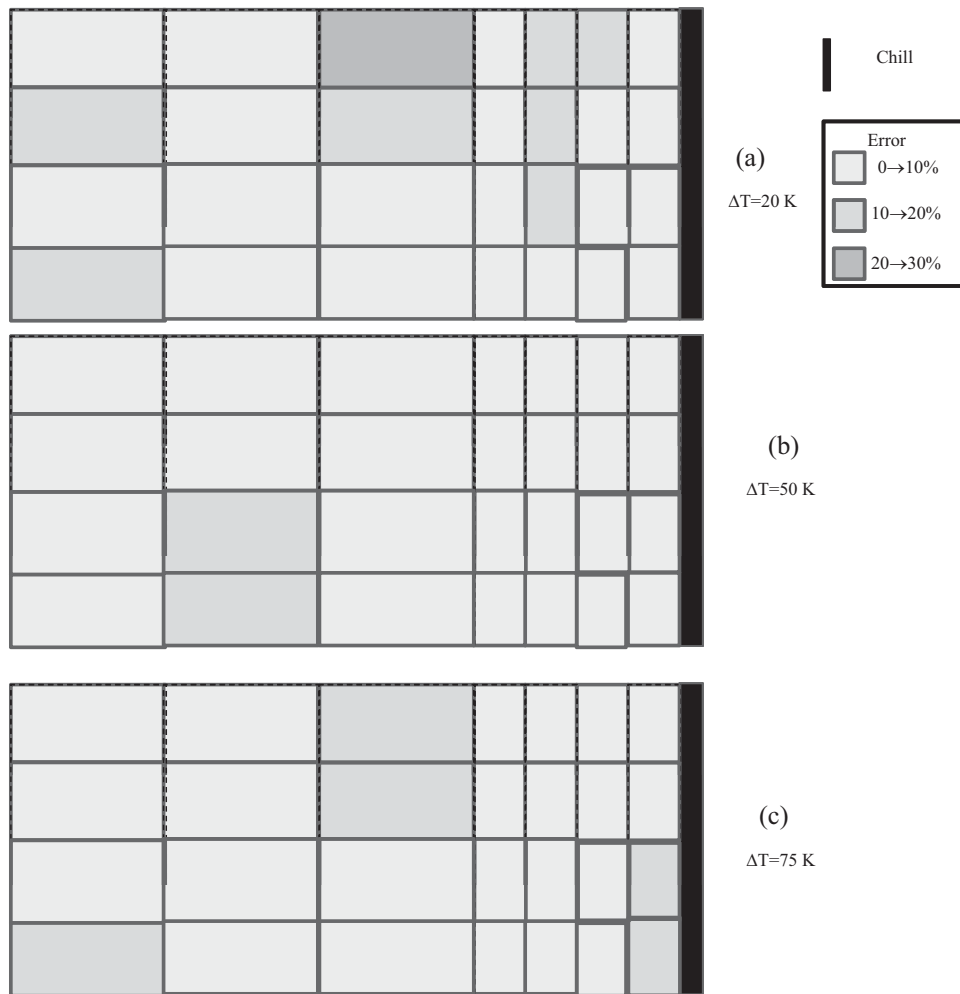
Figure 18. Variation of segregation errors with some diffusion mechanism without interdendritic strain for superheats a) 20 K, b) 50 K, and c) 75 K for Al–4.5% Cu alloy.

histories of different exterior and interior nodes may affect. By comparison these figures, it can been seen also that the errors change from maximum values associated with complete diffusion mechanism, see Figure 4a–c, into minimum error values with some diffusion mechanism ($\alpha^* = 0.25$), see Figure 6a–c, through intermediary error values of no diffusion mechanisms shown in Figure 5a–c for all superheats. This is due to differences in the terms of local solute segregation Equations T-2-2, T-2-3, and T-2-4 illustrated in Table 2. These terms control the calculations of macrosegregation distributions under the same casting and cooling conditions. This means that some alloys follow the complete diffusion mechanism and exhibit low macrosegregation whereas other alloys are controlled by no diffusion mechanism or some diffusion mechanism with various instantaneous diffusion parameter values ''α^*'' and reveal higher macrosegregation than the first mechanism based on the value of instantaneous diffusion parameter where α^* takes values from 0 for no diffusion mechanism to 0.5 for complete diffusion mechanism in dendritic solid.

The model results in Figure 17a–c exhibit the effect of mushy permeability on the macrosegregation distribution with some diffusion mechanism in dendritic solid for 20, 50, and 75 K superheats, respectively. From these predications, it is shown that segregation errors reveal positive and increase for all cast ingots where this increasing is higher in the exterior nodes than interior nodes. This is because of the difference in the cooling rate and the mushy width between the different node locations. Another interesting observed result arises from the examination of these predications where the positive increasing in segregation error is not uniform between the top, intermediate, and bottom nodes. This is due to natural and direction of convection streams of control volume elements of these nodes.[29,30,43] From this examination, it is shown generally that the effect of mushy permeability on segregation error is positive, significant and its average values between 8.5% into

2.67% for top exterior and interior nodes, respectively. However, in the bottom nodes, these values changes from 3.87 of exterior nodes into 1.88% for interior nodes. Therefore, the comparisons between these results and grain densities shown in Figure 17a–c indicate that the effect of mushy permeability on the segregation errors is inversely proportion with grain density.[29,30]

Figure 18a–c presents the effect of interdendritic strain on the macrosegregation distribution with some diffusion mechanism in dendritic solid for 20, 50, and 75 K superheats, respectively. In these figures, the predications indicate that the effect of interdendritic strain is not uniform and slight on the changes in the segregation errors. The changes in the segregation errors vary from small positive changing from 0.875, 2, and 1.6% for top exterior node to 0.64%, 1.12, and 0.23 for bottom exterior nodes with 20, 50, and 75 superheats, respectively. Also, this increasing in the positive errors decreases from the maximum changing value 2% for exterior nodes into minimum value 0.03% for interior nodes. These small differences are due to the type of structure, natural and small magnitudes of interdendritic strain with uniform and slow cooling rate during dendritic solidification process.

In general, these model predications show the importance of the selection of diffusion mechanism, accurate calculations of mushy permeability, and interdendritic strain[15,51] on the explanations and studies of macrosegregation phenomena and its effect on different defects during dendritic solidification. This may explain the mechanism of extruded surface segregation layer in aluminum direct chill casting process with interdendritic strain tensile followed by compressed distributions.[14,33] It may also illustrate the effect of crystal distortion on this phenomenon due to steep segregation during dendritic equiaxed solidification process and therefore the mechanism of interdendritic crack formation in nonferrous alloys due to increasing in the interdendritic areas.[14] Also, it may be shed some of light on the mechanism of brittle-ductile temperature range during solidification with interdendritic crack formation in steel processes.[52–54] This may be due to steep variation in the local macrosegregation in the interdendritic liquid and then the precipitous micro-segregation distribution in the steel dendrites.[55]

5. Summary and Concluded Remarks

The effect of melt superheats on the mushy permeability, interdendritic strain generation and therefore, on the macrosegregation distributions during dendritic solidification has been successfully characterized experimentally and numerically. This was achieved through the development of a two-dimensional mathematical and numerical model that was utilized to predict heat flow, thermal convection streams, interdendritic strain, and macrosegregation under different diffusion mechanisms. In order to verify the model predications, laboratory-scale apparatus was designed and experimental were carried out by a static horizontal steel chill mould by using water cooling. The model was validated with experimental cooling curves in different location in the casting as well as with macrosegregation measurements. The effects of different diffusion mechanisms in dendritic solid, mushy permeability, and interdendritic strain on the errors in predicted macrosegregation results also were studied and discussed. From the results of this investigation, the following conclusions can indicate unambiguously that;

(1) the diffusion mechanism in dendritic solid plays an important role to from the macrosegregation phenomenon during dendritic solidification processes.
(2) the effect of mushy permeability on macrosegregation distribution is essential and mushy permeability depends considerably on the magnitude of grain density criterion or grain size.
(3) The effect of interdendritic strain in this study is no significant due to small values but the nature of this strain in different mushy regions cannot be neglected.

Although, the results of macrosegregation simulations, combined with knowledge of dendritic solidification phenomena, may lead to a consistent mechanism for the formation of some solidification defects, it is necessary to create more investigations by both experimental and numerical modeling to refine the model, solve the remaining problems and to apply the solutions techniques in the global metallic industries especially in steel industry. Another important aspect of the future work is to simulate these techniques to face the practical requirements in metallic industries and to explain accurately some of complicated mechanisms during casting processes.

steel research
international

FULL PAPER

Nomenclature

A	elementary area (m^2)
a, b	constants in Equation T-3-2)
$\underline{C}$	concentration of solute (wt%)
$\bar{E}$	average energy capacity ($W\,s\,m^{-3}$)
E	internal energy ($W\,s\,m^{-3}$)
E_{tr}	imparted heat conduction energ ($W\,s\,m^{-3}$)
E_{in}	liberated inner heat energy ($W\,s\,m^{-3}$)
f	fraction constant in Equations T-3-1 and T-3-2
g	gravity acceleration ($m\,s^{-3}$)
$h(t)$	Newtonian heat-transfer coefficient at time t ($W\,m^{-1}\,k^{-1}$)
$\underline{H}$	enthalpy ($kJ\,kg^{-1}$)
H_s	average solid enthalpy ($kJ\,kg^{-1}$)
K^e	equilibrium partition coefficient
k_c	constant in Equation T-3-12
L	latent heat of fusion ($J\,kg^{-1}$)
N_e	number of alloying elements
P	pressure ($N\,m^{-2}$)
Q_ϕ	surface heat flux (($kW\,m^{-2}$)
R_d	radius of equiaxed grain (m)
S_A	grain boundary surface area per unit volume (m)
S_{Cu}	copper macrosegregation ratio
t	time (s)
T	temperature (K)
T_m	melting of pure iron (°C)
T_{lo}, T_{so}	liquidus and solidus temperatures of binary alloy (°C)
T_ϕ, T_w	surface and cooling fluid temperatures (°C)
u	velocity component in x direction ($m\,s^{-1}$)
U	local interdendritic liquid velocity ($m\,s^{-1}$)
V_a	dendritic growth rate ($m\,s^{-1}$)
$V(T)$	volume at temperature T (m^3)
$V(T_{coh})$	volume at coherent temperature T_{coh} (m^3)
w	velocity components in z direction ($m\,s^{-1}$)
x, z	Cartesian co-ordinates (m)

Greek

α	thermal expansion coefficient ($1\,K^{-1}$)
α^*	instantaneous diffusion parameter ($m^2\,s^{-1}$)
β_j	coefficient in Equation T-3-3 for element j
χ_j^l	concentration of element j in the liquid phase (wt pct)
ε	strain
$\varepsilon_x, \varepsilon_z$	strain in the direction x and z, respectively
$\sum \varepsilon_i$	total change in strain per unit volume
κ	permeability
λ	thermal conductivity ($w\,m^{-2}\,K^{-1}$)

μ	viscosity ($kg\,m^{-1}\,s^{-1}$)
ρ	density ($kg\,m^{-3}$)
$\bar{\rho}$	average density ($kg\,m^{-3}$)
ψ_j	coefficient in Equation T-3-4 for element j
Δ	infinitesimal element length or time

Superscripts

$l \to s$	phase transformation from liquid to solid
$i \to j$	phase transformation from solid phase i to j

Subscripts

coh	coherent
conv	convection stream
eff	effective
i	phase
Int	interdendritic liquid
ph	Thermo-metallurgical
l	liquid
s	solid

Greek Subscripts

η	coordinate for the local fraction of solid

References

[1] J. S. Kirkaldy, W. V. Youdelis, *Trans. TMS-AIME* **1958**, *212*, 833.

[2] M. C. Flemings, G. E. Nereo, *Trans. TMS-AIME* **1967**, *239*, 1449.

[3] S. Minakawa, I. V. Samarasekera, F. Weinberg, *Metall. Trans. B* **1985**, *16B*, 595.

[4] K. Kubo, R. D. Pehlke, *Metall. Trans. B* **1985**, *16B*, 359.

[5] D. R. Poirier, K. Yeumand A. L. Maples, *Metall. Trans. A* **1987**, *18A*, 1979.

[6] J. Ampuero, A. Hoadley, M. Rappaz in *Proceed Modelling of Casting Welding Advanced Solidification Processes* (Eds: V.M. Rappaz, M. Ozgu, K. Mahin,), TMS, Warrendale, PA, USA **1991**, p. 449.

[7] J. Ni, C. Beckermann, *Metall. Trans. B* **1991**, *22B*, 349.

[8] M. El-Bealy, H. Fredriksson, *Metall. Trans. B.* **1996**, *27B*, 999.

[9] M. El-Bealy, H. Fredriksson, *Scand. J. Metall.* **1994**, *23*, 140.

[10] M. El-Bealy, *Metall. Trans. B* **2000**, *31B*, Parts I & II, 331 & 345.

[11] H. Fredriksson, A. Olsson, *Mater. Sci. Technol.* **1986**, *2*, 33.

[12] J. Szekely, *Fluid Flow in Phenomena Metals Processing*, Academic Press, New York, London **1979**, p. 64.

[13] D. R. Poirier, P. J. Nandapurkar, S. Ganesan, *Metall. Trans. B* **1991**, *22B*, 889.

[14] M. O. El-Bealy, in *Proced. of Light Metals, TMS-Annual Meeting, "Cast Shop Technology"*, Seattle, Washington, USA, 2010, pp. 683–688.

[15] M. O. El-Bealy, Macrosegregation and Interdendritic Cracks in Steel Casting Processes, Ph. D. Thesis, Royal Institute of Technology, Stockholm, Sweden 1995.

[16] J. M. Drezet, G. Eggeler, *Scripta Metall. Trans.* **1994**, *31*, 757.

[17] C. Li, B. G. Thomas, *Metall. Trans. B* **2004**, *35B*, 1151–1172.

[18] S. Ganesan, D. R. Poirier, *Tech. Commun. Metal. Trans. A* **1987**, *18A*, 721.

[19] B. Rogberg, High Temperature Properties of Steels and their Influence on the Formation of Defects in Continuous Casting, Ph. D. Thesis, Royal Institute of Technology, Stockholm, Sweden 1982.

[20] E. Scheil, *Metallforschung* **1947**, *2*, 69.

[21] M. O. El-Bealy, Some Fundamentals Aspects of Two-Phase Region For Dendritic Solidification of carbon and Low Alloyed Steel Casting Processes, Tech. Report, University of Illinois at Urbana-Champaign/MIE, 1996.

[22] D. P. Ziegler, Alcoa Technical Center, Alcoa Center, PA, private communication, 1994.

[23] G. Chai, L. Backnart, T. Rølland, L. Arnberg, *Metall. Trans. A* **1995**, *26A*, 965–970.

[24] A. Jablonka, K. Harste, K. Schwerdrfeger, *Steel Res.* **1991**, *62*, 24–29.

[25] S. N. Tewari, R. Tiwari, *Metall. Trans. A* **2003**, *34A*, 2365.

[26] T. S. Piwonka, M. C. Flemings, *Trans. AIME* **1966**, *236*, 1157.

[27] A. V. Reddy, C. Beckermann, *Metall. Trans. B* **1997**, *28B*, 479.

[28] S. V. Patanker, *Numerical Heat Transfer and Fluid flow*, Hemisphere Publication Corporation, New York **1980**.

[29] C. Y. Wang, S. Ahuja, C. Beckermann, H. C. De Groh III, *Metall. Trans. B* **1995**, *26B*, 111.

[30] C. Beckermann, C. Y. Wang, *Metall. Trans. A* **1996**, *27A*, 2784.

[31] N. A. El-Mahallawy, A. M. Assar, *J. Mater. Sci.* **1991**, *26*, 1729.

[32] C. A. Muojekwu, I. V. Samarasekera, J. K. Brimacombe, *Metall. Trans. B* **1995**, *26B*, 361.

[33] M. O. El-Bealy, *Can. Metall. Q* **2010**, *49*, 47.

[34] M. O. El-Bealy, R. M. Hammouda, *Steel Res. Int.* **2007**, *78*, 602.

[35] L. D. J. Sully, *AFS Trans.* **1976**, *84*, 735.

[36] N. A. Shah, J. J. Moore, *Metall. Trans. B* **1989**, *20B*, 893.

[37] H. Mizukami, *Iron Steel Inst. Jpn.* **1991**, *4(1)*, 287.

[38] K. Ho, R. D. Pehlke, *Metall. Trans. B* **1985**, *16B*, 585.

[39] M. O. El-Bealy, Proceed. 6th European Conference on Continuous Casting, 3–6 June 2008-Riccione, Italy, 2008.

[40] J. K. Brimacombe, K. Sorimachi, *Metall. Trans. B* **1977**, *8B*, 489.

[41] J. K. Brimacombe, *Can. Metall. Q* **1976**, *15*, 163.

[42] M. El-Bealy, Proceed. Of 84th Steelmaking Conf., 25–28 March, Baltimore, MD, USA, 2001.

[43] J. K. Brimacombe, F. Weinberg, E. A. Hawbolt, *Metall. Trans. B* **1979**, *10B*, 279.

[44] B. G. Thomas, I. V. Samarasekera, J. K. Brimacombe, *Metall. Trans. B* **1988**, *19B*, Parts I & II, 277 & 289.

[45] R. C. Weast, *Handbook of Chemistry and Physics*, Chemical Rubber Publishing Co. Cleveland, Ohio **1971**.

[46] G. Li, B. G. Thomas, *Metall. Trans. B* **2004**, *35B*, 1151.

[47] C. Y. Wang, C. Beckermann, *Metall. Trans. A* **1996**, *27A*, Parts I & II, 2754 & 2765.

[48] W. Reif, *Nucleation Separation Theory and Natural Convection Streams During Dendritic Equiaxed Solidification Processes*, Institut fur Metallforsung Metallkunde, TU-Berlin, Geramny **1989**.

[49] C. Y. Wang, C. Beckermann, *Metall. Trans. A* **1993**, *24A*, 2787.

[50] A. Ohno, *Solidification*, Springer-Verlag Berlin, Heidelberg, New York **1987**.

[51] M. O. El-Bealy, *Metall. Trans. B* **2011**, *42B*, 1280–1296.

[52] W. T. Lankford, *Metall. Trans.* **1972**, *3*, 1331.

[53] J. K. Brimacombe, F. Weinberg, B. Hawbolt, *Metall. Trans. B* **1979**, *10B*, 279.

[54] M. O. El-Bealy, *Metall. Trans. B* **2012**, *43*, 635–656.

[55] Y. Ueshima, S. Mizoguchi, T. Matsumiya, H. Kajioka, *Metall. Trans. B* **1986**, *17B*, 845.